SARS-CoV-2 spike-glycoprotein processing at S1/S2 and S2' and shedding of the ACE2 viral receptor: roles of Furin and TMPRSS2 and implications for viral infectivity and cell-to-cell fusion

Rachid Essalmani[1], Jaspreet Jain[2,7], Delia Susan-Resiga[1,7], Ursula Andréo[1,2,7], Alexandra Evagelidis[1], Rabeb Mouna Derbali[1], David N. Huynh[1], Frédéric Dallaire[2], Mélanie Laporte[2], Adrien Delpal[3], Priscila Sutto-Ortiz[3], Bruno Coutard[4], Claudine Mapa[5], Keith Wilcoxen[5], Etienne Decroly[3], Tram NQ Pham[2], Éric A. Cohen[2,6*] & Nabil G. Seidah[1*]

[1] **Laboratory of Biochemical Neuroendocrinology Montreal Clinical Research Institute** (IRCM, affiliated to the Univ. of Montreal) 110 Pine Ave west, Montreal, QC, H2W1R7, Canada

[2] **Laboratory of Human Retrovirology Montreal Clinical Research Institute** (IRCM, affiliated to the University of Montreal) 110 Pine Ave west, Montreal, QC, H2W1R7, Canada

[3] **AFMB, CNRS**, Université Aix-Marseille, CNRS, UMR 7257, Case 925, 163 Avenue de Luminy, 13288 Marseille Cedex 09, France, Marseille, France

[4] **Unité des Virus Émergents** (UVE: Aix-Marseille Univ - IRD 190 - **Inserm** 1207 - IHU Méditerranée Infection), Marseille, France

[5] **Boston Pharmaceuticals,** Translational Research, 55 Cambridge Parkway, Suite 400, Cambridge, MA 02142, USA

[6] **Department of Microbiology, Infectiology and Immunology**, Université de Montréal, Montréal, Québec, Canada

[7] Each of these authors contributed equally: Jaspreet Jain, Delia Susan-Resiga and Ursula Andreo

[*]Corresponding authors: seidahn@ircm.qc.ca; eric.cohen@ircm.qc.ca

Short title: **Furin & TMPRSS2: spike cleavage & SARS-CoV-2 infection**

ABSTRACT

The spîke (S)-protein of SARS-CoV-2 binds ACE2 and requires proteolytic "priming" at P**R**RA**R**$_{685}$↓ into S1 and S2 (cleavage at S1/S2), and "fusion-activation" at a S2' site for viral entry. *In vitro,* Furin cleaved peptides mimicking the S1/S2 cleavage site more efficiently than at the putative S2', whereas TMPRSS2 inefficiently cleaved both sites. In HeLa cells Furin-like enzymes mainly cleaved at S1/S2 during intracellular protein trafficking, and S2' processing by Furin at KPS**KR**$_{815}$↓ was strongly enhanced by ACE2, but not for the optimized S2' KRRKR$_{815}$↓ mutant (μS2'), whereas individual/double KR815AA mutants were retained in the endoplasmic reticulum. Pharmacological Furin-inhibitors (Boston Pharmaceuticals, BOS-inhibitors) effectively blocked endogenous S-protein processing in HeLa cells. Furthermore, we show using pseudotyped viruses that while entry by a "pH-dependent" endocytosis pathway in HEK293 cells did not require Furin processing at S1/S2, a "pH-independent" viral entry in lung-derived Calu-3 cells was sensitive to inhibitors of Furin (BOS) and TMPRSS2 (Camostat). Consistently, these inhibitors potently reduce infectious viral titer and cytopathic effects, an outcome enhanced when both compounds were combined. Quantitative analyses of cell-to-cell fusion and spîke processing revealed the key importance of the Furin sites for syncytia formation. Our assays showed that TMPRSS2 enhances fusion and proteolysis at S2' in the absence of cleavage at S1/S2, an effect that is linked to ACE2 shedding by TMPRSS2. Overall, our results indicate that Furin and TMPRSS2 play synergistic roles in generating fusion-competent S-protein, and in promoting viral entry, supporting the combination of Furin and TMPRSS2 inhibitors as potent antivirals against SARS-CoV-2.

IMPORTANCE

SARS-CoV-2 is the etiological agent of COVID-19 that resulted in >5 million deaths. The spike protein (S) of the virus directs infection of the lungs and other tissues by binding the angiotensin-

converting enzyme 2 (ACE2) receptor. For effective infection, the S-protein is cleaved at two sites: S1/S2 and S2'. Cleavage at S1/S2, induces a conformational change favoring the recognition of ACE2. The S2' cleavage is critical for cell-to-cell fusion and virus entry into host cells. Our study contributes to a better understanding of the dynamics of interaction between Furin and TMPRSS2 during SARS-CoV-2 entry and suggests that the combination of a non-toxic Furin inhibitor with a TMPRSS2 inhibitor could significantly reduce viral entry in lung cells, as evidenced by an average synergistic ~95% reduction of viral infection. This represents a powerful novel antiviral approach to reduce viral spread in individuals infected by SARS-CoV-2 or future related coronaviruses.

INTRODUCTION

Epidemics date from prehistoric times but are exacerbated by overcrowding and human impact on the ecosystem (1). The RNA coronaviruses (CoV) are zoonotic pathogens that occasionally spread in the human population, causing respiratory, enteric, renal, and neurological diseases (2). Electron microscopy of CoV revealed that the lipid envelope of each virion is surrounded by a "crown"-like structure (3), composed of multiple copies of a viral surface glycoprotein known as "spike" (S), which is essential for receptor binding and virus entry. Severe Acute Respiratory Syndrome coronavirus (SARS-CoV-1) and Middle East Respiratory Syndrome coronavirus (MERS-CoV) are infectious pathogenic viruses that appeared in humans at the beginning of the 21st century (2, 4). At the end of 2019, a third CoV, namely SARS-CoV-2, emerged causing widespread respiratory and vascular illnesses (5), coined COVID-19 (6).

Like envelope glycoproteins of many infectious viruses (7-9), the secretory type-I membrane-bound S of SARS-CoV-2 is synthesized as a precursor (proS) that undergoes post-transcriptional cleavages by host cell proteases at specific sites to allow viral entry. During infection, the trimeric proS (monomer, 1,272 residues) is first processed at an S1/S2 cleavage site (Fig. 1A). Unlike SARS-CoV-

72 1, the S-protein of SARS-CoV-2 exhibits an insertion of four critical amino acids (PRRA) at the S1/S2
73 junction (10-12), forming a canonical P**R**RA**R**$_{685}$↓ Furin-like cleavage site (FCS). Such "priming"
74 step divides the protein into two subunits S1 and S2 held together by non-covalent interactions.
75 Following S-protein priming, the N-terminal S1-ectodomain undergoes a conformational change that
76 exposes its receptor-binding-domain (RBD) (13), which recognizes the ACE2 entry receptor (11). The
77 S2-subunit, which is responsible for the fusogenic activity of the spike-S glycoprotein, contains an
78 additional "fusion-activation" proteolytic site (S2') followed by an α-helical fusion peptide (FP) and
79 two heptad-repeat domains (HR1 and HR2) preceding the transmembrane domain (TM) and cytosolic
80 tail (CT) (Fig. 1A). It is thought that cleavage at S2' triggers large-scale rearrangements, including a
81 refolding step that is associated with the separation of S1- and S2-subunits and exposure of the
82 hydrophobic α-helix FP, favoring fusion of viral and host cell membranes leading to virus entry (14).
83 Fusion with host cells can occur either at the cell surface (pH-independent) or with internal
84 membranes following endocytosis (pH-dependent) (15). However, the cognate host-cell proteases
85 responsible for the S1/S2 and S2' cleavages vary between coronaviruses and cell types (11, 12, 16-
86 19).

87 The proprotein convertases (PCs; genes *PCSKs*) constitute a family of nine secretory serine
88 proteases that regulate various processes in both health and disease states (20). Through
89 proteolysis, PCs are responsible for the activation and/or inactivation of many secretory precursor
90 proteins, including virus/pathogen surface glycoproteins (9, 20). Seven PCs, including the widely
91 expressed Furin, PC5A, PACE4 and PC7, cleave secretory substrates at specific single/paired basic
92 amino acids (aa) within the motif (K/R)-X_n-(K/R)↓, where Xn= 0, 2, 4 or 6 spacer X residues (20).
93 Because of their critical functions, PCs, especially Furin (21), are implicated in many viral
94 infections by inducing specific cleavages of envelope glycoproteins, a condition that allows not

95 only the fusion of the viral lipid envelope with host cell membranes (9, 20), but can also lead to
96 cell-to-cell fusion (syncytia), especially for viruses that undergo pH-independent fusion (22, 23).
97 As the S1/S2 cleavage of SARS-CoV-2 is thought to play a critical role for cellular receptor
98 recognition and virus entry, the efficacy and extent of this activation step by host proteases might
99 be a key determinant regulating cellular tropism, viral pathogenesis, and human-to-human
100 transmission. In contrast to SARS-CoV-1, the proS of SARS-CoV-2 contains a structurally
101 exposed P**R**RA**R**$_{685}$↓S**V** motif (10, 11) (Fig. 1A), which corresponds to a canonical FCS (9, 10,
102 20). This Furin-like motif is presumably cleaved during *de novo* virus egress (23) for S-protein
103 priming and may play a key role for the efficient spread of SARS-CoV-2 to various human tissues
104 compared to the more limited tropism of other lineage B β-coronaviruses (10, 24). Furthermore,
105 based on the predicted S2' KPS**KR**$_{815}$↓S**F** sequence of SARS-CoV-2, we proposed (10) that Furin-
106 like enzymes could also cleave at this S2' site (Fig. 1A). Indeed, various reports have since
107 supported the implication of Furin in the S1/S2 priming of the S-protein in human cell culture
108 models (12, 25, 26) and *in vivo* in mice, hamsters and ferrets (27, 28). In addition, it was also
109 suggested that the cell surface type-II transmembrane serine protease 2 (TMPRSS2) can enhance
110 fusion by cleavage at S2', but that S1/S2 cleavage is mostly Furin-dependent (18). The ability of
111 the Arg/Lys-specific TMPRSS2 (29, 30) to directly cleave at S2' was suggested based on the viral
112 entry blockade by the TMPRSS2 inhibitor Camostat (31-33), and through silencing of TMPRSS2
113 expression using a morpholino oligomer (18), but direct evidence of its involvement in such spike
114 protein processing at S2' is still lacking. Thus, it is likely that one or more proteases regulate
115 SARS-CoV-2 entry into human airway epithelial cells (18, 24). Furthermore, since the tissue-
116 expression of TMPRSS2 is restricted to a limited set of cell types compared to that of the
117 ubiquitously expressed Furin, the activity of the latter may widen viral tropism (34).

118 Thus, the major goals of the present study were to precisely define the respective roles of Furin and
119 TMPRSS2 in the fusion activation, and to test the consequences of their inhibition on SARS-CoV-2
120 infectivity and S-mediated cell-to-cell fusion. Herein, using a multi-disciplinary approach, we provide
121 mechanistic evidence supporting a critical role of the proprotein convertase Furin in the processing of
122 SARS-CoV-2 spike protein. Specifically, we map the exact S2' processing site by proteomics and
123 highlight by mutagenesis the functional importance of S1/S2 and S2' regions in viral entry and cell-
124 to-cell fusion. For the first time, we demonstrate that three novel cell-permeable small molecules
125 inhibitors of proprotein convertases developed by Boston Pharmaceuticals, referred hereafter as BOS-
126 inhibitors, can potently inhibit proS processing at S1/S2 and S2' by endogenous Furin-like proteases
127 leading to efficient inhibition of viral entry, viral replication, and cell-to-cell fusion. Finally, our work
128 sheds a new light on the role of TMPRSS2 in promoting ACE2 shedding and enabling S2' processing,
129 thereby leading to enhanced cell-to-cell fusion.
130
131 **RESULTS**
132 **Comparative analysis of cleavage of SARS-CoV-2 peptides mimicking S1//S2 and S2'**
133 **processing sites by Furin and TMPRSS2.** Furin is thought to be important in the processing of
134 SARS-CoV-2 spike-glycoprotein (S) at the S1/S2 site (10, 24) while TMPRSS2 has been proposed to
135 have an important role in activating S at S2' (18, 31-33) (Fig. 1A). Nevertheless, the relative
136 contributions of Furin and TMPRSS2 towards cleavage of SARS-CoV-2 S glycoprotein at both sites
137 remain poorly defined. Thus**,** the susceptibility of SARS-CoV-2 S glycoprotein to Furin-cleavage
138 was first assessed *in vitro*. Incubation of quenched fluorogenic peptides encompassing S1/S2 and
139 S2' sites (Supporting Information SI-Table 1) demonstrated that the S1/S2 site of SARS-CoV-2 S
140 was efficiently cleaved by 2 nM Furin at pH 7.5 (Fig. 1B), whereas the S1/S2 site of SARS-CoV-1,
141 which lacks an FCS, was not cleaved (Fig. 1B). Furin less efficiently cleaved the SARS-CoV-2-mimic

142 peptide at S2', requiring 50-fold higher enzyme concentrations (100 nM) to detect cleavage (inset Fig.
143 1B). The high specificity of the SARS-CoV-2 for processing at Furin-like motifs was next confirmed
144 by demonstrating that substitutions of basic residues at the S1/S2 cleavage site (RRA**A**$_{685}$↓S,
145 **A**RA**A**$_{685}$↓S, **A**RAR$_{685}$↓S) dramatically impaired S1/S2 cleavage (Fig. 1B). Altogether, these data
146 demonstrate that *in vitro* Furin best cleaves at S1/S2 and less efficiently at S2'. In contrast, TMPRSS2
147 did not efficiently cleave the S1/S2 and S2' peptides (Fig 1C). The cleavage at S1/S2 became
148 detectable only when TMPRSS2 was present at high concentration (50 nM). However, different from
149 Furin, under this condition TMPRSS2 cleavage of peptides mimicking the S1/S2 Ala-mutants RRAA,
150 ARAA and ARAR and S2' was also evident (Fig. 1C). Taken together, these data emphasize the
151 critical importance of the P1 and P4 Arg for Furin-mediated cleavage at S1/S2 and suggest that the
152 likely Arg-motif recognized by TMPRSS2 is either (Ala/Arg)-Arg↓Ala or Ala-Arg↓Ser with a
153 preference for Ala at P2 over Arg, and Ala or Ser at P1'.
154
155 **Furin and Furin-like proteases can process proS at S1/S2 and S2' sites.** To examine the ability
156 of Furin and Furin-like enzymes to process the precursor proS of SARS-CoV-2 *in cellulo,* we used a
157 HeLa cells model, which endogenously express Furin but not TMPRSS2 or ACE2 (*not shown*), as
158 reported earlier (35). Here, we found that endogenous enzymes efficiently processed a V5-tagged proS
159 (Fig. 1A), likely at the S1/S2 junction to generate a ~100 kDa S2-like fragment (Fig. 2A). Interestingly,
160 when the proprotein convertases PC5A, Furin, PC7 or PACE4 were transiently overexpressed,
161 cleavage at this site became more prominent. Of note, a partial knockdown of Furin decreased S2
162 levels by more than 60% (SI-Fig. 1A). Furthermore, it was only when Furin or PC5A were
163 overexpressed that cleavage at a potentially S2' site was noticeable, yielding a ~75 kDa fragment (Fig.
164 2A). The remaining ~200 kDa proS$_{im}$ corresponded to an immature precursor form that had not exited
165 the ER, as attested by its sensitivity to both endoglycosidase-F and endoglycosidase-H (SI-Fig. 1B)

166 and insensitivity to Furin-like convertases, which are only active in the TGN and/or cell
167 surface/endosomes (20, 36).

168 To precisely define the ~100-kDa fragment, we mutated the S1/S2 site **R**RA**R**$_{685}$↓S and found that
169 the double Ala-mutant [**A**RA**A**$_{685}$] (denoted μS1/S2) abrogated processing at S1/S2 and putative S2'
170 (Fig. 2B), highlighting once again the importance of the P4- and P1-Arg for recognition by Furin-like
171 enzymes (20). The loss of Furin-like cleavage at S1/S2 resulted in accumulation of a higher molecular
172 size band (~230 kDa), representing mature proS, that exited the endoplasmic reticulum (ER), as
173 confirmed by its resistance to endoglycosidase-H, while still sensitive to endoglycosidase-F digestion
174 (SI-Fig. 1B).

175 To further define the Arg-residues critical for processing at S1/S2, we assessed the effect of single
176 residue mutations: R682A, R685A and S686A and confirmed the critical importance of P1-Arg$_{685}$ or
177 P4-Arg$_{682}$ for the generation of S2 by endogenous Furin (SI-Fig. 1C). However, unlike μS1/S2 (Fig.
178 2B), these single mutants were partially cleaved by overexpressed Furin (SI-Fig. 1C), reflecting the
179 multi-basic nature of the S1/S2 recognition sequence and suggesting the importance of the P3 Arg$_{683}$
180 (37). The S686A mutant was based on the prediction that Ser$_{686}$ could be O-glycosylated (38), which
181 may hamper processing at S1/S2 (39). However, like the WT-S, the S686A mutant was efficiently
182 processed by Furin into S2 and S2' (SI-Fig. 1C), suggesting the lack of O-glycosylation at Ser$_{686}$ in
183 HeLa cells.

184 We next used site-directed mutagenesis to identify the exact S2' site cleaved by Furin. However,
185 K814A, R815A and K814R815A mutants at P1 and P2 residues (20) of the predicted S2' site
186 (KPSKR$_{815}$↓SF) altered S-protein trafficking resulting in a predominantly ER-retained proS$_{im}$
187 protein, especially for the R815A and the double mutant (SI-Fig. 1D). Therefore, we resorted to
188 mass spectrometry analysis of proteins migrating at the S2' position to unambiguously identify
189 this site. The peptides generated by a Lys-specific protease (K$_{814}$↓) allowed for the discrimination

190 between SFIEDLLFN$\underline{K}_{825}$ that would be generated if Furin cleaved at Arg_{815}, and
191 $\underline{R}_{815}$SFIEDLLFN$\underline{K}_{825}$ that would be derived from N-terminally extended proteins, e.g., S2.
192 Proteomic data (Fig. 2C) revealed a >50-fold higher ratio of $\underline{S}$FIEDLLFN$\underline{K}_{825}$ to
193 $\underline{R}$SFIEDLLFN$\underline{K}_{825}$ for the S2' product, demonstrating that the N-terminus of S2' starts at Ser_{816}
194 and that Furin cleaves after Arg_{815}↓ in the sequence KPSK$\underline{\mathbf{R}}_{815}$↓SFIEDLLFNKVT (Fig. 1A). To
195 further demonstrate the role of Furin in S2' cleavage we generated a Furin-optimized S2' site
196 (called μS2') with a polybasic sequence K$\underline{RR}$KR_{815}↓SF in proS and found that this derivative was
197 very efficiently cleaved by endogenous and especially by overexpressed Furin, yielding a similar
198 ~75 kDa fragment (Fig. 2D). Altogether, these data demonstrate that the S2' cleavage occurs at
199 Arg_{815}↓ and further reveal that this site can be partially processed by overexpressed Furin and/or
200 PC5A.
201
202 **Processing at S2' by Furin is enhanced in the presence of ACE2.** Immunocytochemical
203 analyses of HeLa cells co-expressing S or μS1/S2-S and ACE2 showed that both S-proteins and ACE2
204 co-localized at the cell surface independent of the state of proS processing (SI-Fig. 2). Given that
205 binding of SARS-CoV-2 S-trimer to the dimeric ACE2 receptor has been proposed to trigger a
206 conformational change in S1, promoting cleavage at S2' (13, 40), we next examined whether this
207 phenomenon would effectively increase/promote S2' processing by Furin. To this end, we expressed
208 the V5-tagged proS spike protein together with ACE2 and Furin in HeLa cells. We found that while
209 not significantly affecting S1/S2 cleavage, ACE2 expression seemed to stabilize the S2 subunit and to
210 strongly enhance the generation of S2' by endogenous and overexpressed Furin (Fig. 3A). Amazingly,
211 in the presence of ACE2, the μS1/S2-S, which is otherwise resistant to cleavage at S1/S2 by
212 endogenous or overexpressed Furin (Fig. 2B), can be partially cleaved directly into S2' by

213 overexpressed Furin (Fig. 3B, last lane). Taken together, we conclude that binding of S-protein to
214 ACE2 likely facilitates exposure of the S2' site (41), thereby enhancing Furin processing at S2'.
215
216 **Furin-inhibitors block S1/S2 and S2' cleavages.** Given the importance of Furin in proS
217 processing at the S1/S2 and S2' sites, we next evaluated the activity of three novel non-toxic, cell-
218 permeable Furin-like inhibitors developed by Boston Pharmaceuticals available as oral (BOS-981,
219 BOS-318) or inhalable (BOS-857) formulations (Fig. 4A). Accordingly, we first tested *in vitro* the
220 efficacy and selectivity of these inhibitors on purified soluble forms of Furin, PC5A, PACE4 and
221 PC7 using a quenched fluorogenic substrate FAM-Q**R**V**RR**AVGIDK-TAMRA. As shown, the
222 inhibitors effectively blocked substrate processing by all convertases with an IC_{50} of ~7-9 nM
223 compared to ~9-10 nM for the known cell-permeable PC-inhibitor decanoyl-RVKR-
224 chloromethylketone (dec-RVKR-cmk) (42, 43) (Fig. 4B). The Furin S1/S2 cleavage was also
225 validated using a 12-residue quenched fluorogenic substrate DABSYL/Glu-TNSP**RR**A**R**↓SVAS-
226 EDANS mimicking the S1/S2 priming site. The inhibition deduced after hill-plot curve fitting (Fig.
227 4C) gave an estimated IC_{50} of 4 ± 0.7 nM for BOS-981, 32 ± 4 nM for BOS-857 and 35 ± 5 nM
228 for BOS-318. As well, BOS-inhibitors inhibited endogenous Furin-like processing of a dibasic
229 bone morphogenic protein 10 (BMP10)-mimic (43) with an IC_{50} of ~8 nM *versus* 5 nM for the
230 dec-RVKR-cmk as determined by a cell-based Golgi imaging assay with U2OS cells (Fig. 4D).
231 We further showed that BOS-inhibitors efficiently blocked S1/S2 and S2' processing by
232 endogenous Furin-like enzymes, resulting in a near complete inhibition at 0.3 μM, also obtained
233 with 50 μM of dec-RVKR-cmk (RVKR; Fig. 4E). Overall, our data clearly demonstrate a role of
234 Furin in the processing of proS at the S1/S2 and S2' sites.
235

236 **Furin-like inhibitors reduce virus production in SARS-CoV-2-infected cells.** We next
237 examined whether blocking the processing of proS by BOS-inhibitors modulates SARS-CoV-2
238 infection. Indeed, in lung derived Calu-3 cells pretreated with 1 μM BOS-inhibitors for 24h before
239 infection, we observed significantly decreased viral titers at 12, 24 and 48h post-infection (Fig.
240 5A). Importantly, the inhibitory effect was dose-dependent, reducing viral burden up to >30-fold
241 with 1 μM BOS-318 (Fig. 5B; left panel). As well, the IC_{50} and selectivity index (44) of BOS-318
242 were 0.2 μM and 475, respectively (Fig. 5B; right panel). Importantly, the levels of spike (full
243 length and cleaved S) and nucleocapsid proteins in the supernatant and cells were decreased in a
244 dose-dependent manner (Fig. 5C), underscoring the crucial role played by Furin-like convertases
245 in SARS-CoV-2 infection in this lung epithelial cell model. A similar analysis with BOS-857 and
246 BOS-981 revealed comparable antiviral effects and selectivity index (SI-Figs. 3A, B). In addition,
247 BOS-inhibitors were also evaluated in Vero E6 cells where SARS-CoV-2 entry and infection is
248 established primarily *via* the endocytic pathway (11, 24). In this system and as expected, treatment
249 with BOS-inhibitors led to weaker effect since we observed a decreased virus production by only
250 ~2.6-5.7-fold (SI-Fig. 4), possibly reflecting a role of Furin-like activity in early endosomes (36)
251 for pH-dependent virus entry in Vero cells.
252 Since TMPRSS2 has been proposed to be important for viral entry at the plasma membrane, we
253 next determined whether combining BOS-inhibitors and the TMPRSS2-inhibitor Camostat would
254 have a synergistic effect, leading to a more pronounced antiviral effect in Calu-3. As shown,
255 although these compounds could reduce viral replication individually, their co-treatment resulted
256 in a synergistic inhibition of ~95 ± 2.5% (>70-fold) of progeny infectious viruses (Fig. 5D and SI-
257 Fig. 5), reinforcing the importance of both Furin-like proteases and TMPRSS2 in promoting
258 efficient SARS-CoV-2 infection of Calu-3 cells.

259 **Furin-like inhibitors reduce viral entry by blocking processing of proS during biosynthesis**
260 **and at the viral entry site.** The more dramatic impact observed with Furin-like inhibitors on virus
261 infection of Calu-3 cells *versus* Vero cells suggests that these inhibitors affect mainly the pH-
262 independent entry mechanism. Thus, we next assessed the effect of BOS-inhibitors on viral entry.
263 Using nanoluciferase-expressing HIV particles pseudotyped with WT, μS1/S2 or μS2' S-proteins, we
264 observed that the viral entry of μS1/S2-S pseudovirions is ~10-fold reduced in Calu-3 cells (Fig. 6A).
265 In contrast, all three pseudotyped viruses were at least 10-fold more infectious in HEK293T-ACE2
266 cells, suggesting that S-priming at S1/S2 is required for optimal viral entry in Calu-3 cells, but
267 dispensable or perhaps even less desirable in HEK293T-ACE2 cells (Fig. 6A). Since these findings
268 were similar to those in Vero E6 cells (45), we surmise that viral entry in HEK293T-ACE2 cells was
269 through the same pH-dependent, endocytic route as reported for Vero cells (46, 47). This agrees with
270 the fact that HEK293 cells allow endocytosis of SARS-CoV-2 pseudovirions *via* clathrin-coated
271 vesicles (48). In the case of μS2'-S-expressing viral particles, entry was more efficient in both cell
272 types (compare the same-coloured dots between WT-S and μS2'-S in absence of BOS, Fig. 6A),
273 implying that S cleavage at the S2'optimized Furin-like site could enhance viral entry. When BOS-
274 318 was present during biosynthesis of pseudovirions, processing of WT-S and μS2'-S was blocked
275 (Fig. 6B), leading to reduced viral entry in Calu-3 by ~3.6- to ~12.5-fold, respectively (Fig. 6A). Thus,
276 BOS-318 treatment phenocopied the effect of the μS1/S2 in both cell types. Nevertheless, under this
277 condition viral entry in HEK293T-ACE2 cells was enhanced by ~10-fold for WT-S and ~2-fold for
278 μS2'-S (Fig. 6A), suggesting that viral entry by the pH-dependent pathway does not require FCS
279 processing.
280 Having observed the negative effect of BOS-318 on S processing by particle-producing cells, we
281 asked whether pre-treating target cells with BOS-318 would also affect entry of SARS-CoV-2
282 pseudoparticles. In Calu-3 cells, where viral entry occurs primarily through fusion at the plasma

283 membrane (46), we observed reduced viral entry by ~3.8-fold for WT-S and ~14-fold for μS2'-S (Fig.
284 6C). This emphasizes a significant contribution of Furin to the processing and priming of S at the
285 plasma membrane of Calu-3 cells after ACE2 recognition. The fact that BOS-318 had a more
286 pronounced effect on entry by μS2'-S-containing viral particles was not surprising given the very
287 efficient S2' processing of this mutant by Furin (Fig. 2D). Of note, viral entry by WT-S pseudoparticles
288 was more affected by 100 μM Camostat compared to that by μS2'-S viral particles (Fig. 6C). Here,
289 entry was reduced by ~8.6-fold for WT-S and ~3.2-fold for μS2'-S, suggesting that Furin plays a more
290 prominent role in the entry of μS2'-S *versus* WT-S viral particles. Lastly, the combined pre-treatment
291 of both BOS-318 and Camostat led to a complete block of viral entry, highlighting the importance of
292 both Furin and TMPRSS2 in mediating viral fusion at the plasma membrane.
293
294 **Furin-like inhibitors decrease cell-to-cell fusion and syncytia formation.** To assess whether
295 BOS-inhibitors also affect cell-to-cell fusion, we developed a co-culture assay in which donor HeLa
296 cells express HIV Tat and the fusogenic S-protein, while acceptor HeLa TZM-bl cells express ACE2
297 and Tat-driven luciferase (49) (Figs. 7A). As a proof-of-principle, we showed that when donor HeLa
298 cells expressing HIV gp160 and Tat fused with acceptor cells expressing CD4 (SI-Fig. 6A, panel b),
299 luciferase activity was increased compared to that observed in TZM-bl control cells co-cultured with
300 donor Hela cells expressing only Tat (SI-Fig. 6B). The expression of S-protein alone in donor HeLa
301 cells did not induce fusion with acceptor TZM-bl control cells (SI-Fig. 6B). However, ACE2
302 expression in TZM-bl allowed fusion with HeLa-expressing S-protein (SI-Fig. 6A, panel c; 6B) in a
303 dose-dependent manner (SI-Fig. 6C), but no fusion was observed with μS1/S2-S (SI-Fig. 6A, panel
304 d). Indeed, the linearity of our assay (correlation coefficient of 0.87) validated the use of luminescence
305 as an indicator of cell-to-cell fusion (SI-Fig. 6C). Using this assay, we found that while donor cells
306 expressing WT-S led to syncytia formation (Fig. 6B) and a >10-fold increased cell-to-cell fusion

307 compared to control (empty vector V, no S) cells (Fig. 6C), donor cells expressing μS1/S2-S did not
308 promote any cell fusion even in the presence of ACE2 (Figs. 6C, D). Thus, the μS1/S2-S phenocopies
309 the effect of BOS-inhibitors on cell-to-cell-fusion (Fig. 6C), whereby absence of Furin-activity would
310 not allow fusion and demonstrates a key role of S1/S2 cleavage in S-mediated cell-to-cell fusion.
311 Consistent with this finding, we observed an almost complete loss of cell fusion when donor cells were
312 treated with BOS-inhibitors or the PC-inhibitor decanoyl-RVKR-cmk (RVKR; Fig. 6C) (43),
313 emphasizing the critical role of Furin-cleavage in promoting ACE2-dependent cell-to-cell fusion in the
314 context of acceptor cells that do not endogenously express TMPRSS2, such as HeLa cells. This fusion
315 assay also enabled the assessment of the effects of some worldwide-spreading S-protein variants of
316 SARS-CoV-2, which seem to affect viral traits such as transmissibility, pathogenicity, host range, and
317 antigenicity of the virus (50, 51). Among these, we selected mutants that modify the Pro at the P5
318 position of the S1/S2 site (Fig. 1A), i.e., the P681H and P681R associated with the α- and δ- variants,
319 respectively (9). Our data showed that while the μS2' mutant did not affect cell-to-cell fusion, the
320 P681H and P681R mutants significantly enhanced it by ~2-fold (Fig. 7D), in line with the higher
321 transmissibility of the associated α- and δ- SARS-CoV-2 variants (50, 51) and increased cell-to-cell
322 fusion (52).
323
324 **TMPRSS2 promotes cell-to-cell fusion in the absence of Furin-mediated cleavage at S1/S2.**
325 Having shown the critical role of Furin-cleavage in promoting ACE2-dependent cell-to-cell fusion in
326 HeLa cells that do not express TMPRSS2, we next examined the importance of TMPRSS2 in cell-to-
327 cell fusion given its significant role in viral entry and replication (Figs. 5D and 6C). Thus, we analyzed
328 fusion between donor cells expressing WT-S or μS1/S2-S (double tagged S-protein: HA at the N-
329 terminus and V5 at the C-terminus) and acceptor cells expressing ACE2 in the absence or the presence
330 of TMPRSS2 (Fig. 8). As shown, in the presence of ACE2, TMPRSS2 reduced fusion by ~2.1-fold in

331 the case of WT-S but increased it by ~2.4-fold in the case of μS1/S2-S (Fig. 8A). Under the same
332 conditions, WB analyses showed that for WT-S, the TMPRSS2 expression decreased by ~4-fold (3.8
333 *versus* 0.9) the relative levels of S2 and modestly increased by ~1.5-fold (0.6 *versus* 0.9) the relative
334 levels of S2'. In contrast, for μS1/S2-S, expression of TMPRSS2 increased S2' levels by ~7-fold (0.1
335 *versus* 0.7) without any detectable change in S2 (0.6 *versus* 0.5) (Fig. 8B). Therefore, in the presence
336 of ACE2, the levels of S2 correlate with cell-to-cell fusion in the case of WT-S that is well cleaved at
337 S1/S2 by Furin. In contrast, fusion correlates best with S2' levels, when cleavage at S1/S2 is limited
338 (μS1/S2-S). Interestingly, secretion of the HA-tagged, N-terminal S1 subunit (aa 14-685; Fig. 1A) was
339 more pronounced for WT-S compared to μS1/S2-S (Fig. 8B). Yet, in both cases, the extent of S1
340 release was not modulated by the presence of TMPRSS2, suggesting that TMPRSS2-mediated
341 enhanced fusion of μS1/S2 was not a consequence of altered S1/S2 cleavage (Fig. 8B).
342
343 **Mechanism by which TMPRSS2 promotes cell-to-cell fusion**. To assess whether TMPRSS2
344 promoted cell-to-cell fusion by enhancing S2' cleavage in the complete absence of S1/S2 priming, we
345 generated a new S-derivative lacking all Arg at S1/S2 (Fig. 1), namely μAS1/S2 ($AAAA_{685}$)-S, and
346 hence different from μS1/S2 (Fig. 1C; ARAA mutant), it would not be cleaved by TMPRSS2 or Furin.
347 Cell-to cell fusion was assessed following incubation of cells expressing WT-S or μAS1/S2-S with
348 acceptor cells expressing ACE2 and/or TMPRSS2. In this context, TMPRSS2 reduced fusion of WT-
349 S by ~2.6-fold and enhanced that of μAS1/S2-S by ~3.1-fold (Fig. 9A), as previously observed with
350 the μS1/S2 mutant (Fig. 8A). Camostat completely restored TMPRSS2-reduced fusion with WT-S and
351 largely attenuated the TMPRSS2-enhanced fusion with μAS1/S2 (Fig. 9A). This revealed that in the
352 presence of ACE2, TMPRSS2 could enhance fusion in absence of S1/S2 priming. We next assessed
353 whether this effect could be related to the differential processing of the S protein and/or to ACE2

354 receptor shedding by TMPRSS2. The WB of cell lysates shows that treatment of acceptor cells with
355 Camostat eliminated the TMPRSS2-induced reduction in S2 observed with WT-S (Fig. 9B), yet it did
356 not significantly alter S2' levels either with WT-S or μAS1/S2 (Figs. 9B, C). In contrast, the WB of
357 ACE2 reveal that TMPRSS2 strongly reduced the levels of mature membrane-bound ACE2 migrating
358 at ~120 KDa, without affecting the lower molecular weight protein which correspond to an immature
359 ER-retained form of ACE2 ($ACE2_{im}$, Figs. 9B, C) that is sensitive to endoH digestion (*not shown*).
360 These results show that ACE2 is shed by TMPRSS2, as proposed in earlier studies (33). As expected,
361 we observed that ACE2 shedding by TMPRSS2 is almost completely blocked by Camostat (compare
362 ACE2+TMP lanes DMSO to CAM) (Figs. 9B and C).

363 In contrast, the WB anti ACE2 reveal that TMPRSS2 strongly reduced the levels of mature
364 membrane-bound ACE2 migrating at ~120 KDa, without affecting the lower molecular weight protein
365 which correspond to an immature ER-retained form of ACE2 ($ACE2_{im}$, Figs. 9B, C) that is sensitive
366 to endoH digestion (*not shown*). These results suggest that ACE2 is shed due to TMPRSS2 cleavage
367 as proposed in earlier studies (33). As expected, we observed that this effect of TMPRSS2 on ACE2
368 processing is almost completely blocked by Camostat (compare ACE2+TMP lanes DMSO to CAM)
369 (Figs. 9B and C). Finally, by analysing the release of S1 in the cell culture media we observed that
370 TMPRSS2-induced release into the media of a longer ~175 kDa fragment from μAS1/S2, referred
371 hereafter as $S1_L$ (Fig. 9C), which is not detected in presence of Camostat. The molecular weight of the
372 $S1_L$ indicates that it corresponds to a TMPRSS2 cleavage of μAS1/S2-S at S2' (Fig. 9B).

373 These results suggest that TMPRSS2 modulation of fusion is complex, as TMPRSS2 alters both
374 the integrity of ACE2 receptor, but also participates in S-processing as attested by the release of $S1_L$
375 which corresponds to the N-terminal cleavage product of μAS1/S2-S at S2'. Interestingly, we did not
376 detect an associated increase in S2' levels, suggesting that after cleavage the fusion process occurs and
377 the S2 protein is subsequently degraded, as suggested by a small degradation product seen on WB

378 (arrow in Figs. 9B, C). We surmise that in the presence of ACE2, TMPRSS2 facilitates the secretion
379 of the N-terminal fragment $S1_L$ generated by cleavage at S2'.

380 Our next goal was to further decipher the contribution of ACE2 cleavage by TMPRSS2 and the
381 seemingly opposite effects of TMPRSS2 on fusion activity with WT-S and μAS1/S2-S (and μS1/S2-
382 S). Hence, since TMPRSS2 cleaves at single Arg and Lys residues (53), we tested the effect of multiple
383 Arg/Lys to Ala mutants in segments close to the transmembrane domain of ACE2 (C0 + C4 in Fig.
384 10A), which were previously proposed to limit the TMPRSS2-induced shedding (54). Accordingly,
385 WB analyses (Fig. 10B) revealed that TMPRSS2, but not its Ser* active site S441A mutant (μTMPR,
386 Fig. 10B; SI-Fig. 7) sheds the membrane-bound ~120 kDa WT ACE2, releasing a major ~95 kDa and
387 a minor ~80 kDa form into the media. In contrast, TMPRSS2 primarily generated the ~80 kDa
388 fragment from the ACE2 (C0+C4) mutant. It should be mentioned that in the absence of TMPRSS2
389 the extent of fusion for both WT-S and μAS1/S2-S was comparable between ACE2 (WT) and ACE2
390 (C0+C4). Interestingly, in the context of the ACE2 (C0+C4) receptor mutant, we found that TMPRSS2
391 no longer modulates the fusion of both WT-S and μAS1/S2-S (Fig. 10C). Importantly, and different
392 from WT ACE2 (Figs. 8, 9), TMPRSS2 did not reduce the levels of S2 when ACE2 (C0+C4) was
393 used (Fig. 10D), nor did it reduce fusion (Fig. 10C). Additionally, the TMPRSS2-enhanced secretion
394 of the ~ 175 kDa $S1_L$ fragment in the absence of S1/S2 cleavage (Fig. 9C; SI-Fig. 7), was no longer
395 detected in the media when ACE2 (C0+C4) was expressed on acceptor cells (Fig. 10D), correlating
396 with the lack of fusion of μAS1/S2-S (Fig. 10C). Altogether, these results suggest for the first time that
397 in the absence of Furin-mediated priming of S, TMPRSS2 promotes cell-to-cell fusion by generating
398 a ~95 kDa sACE2 that likely binds the $S1_L$ cap (55) and favors its release.

399

400

401

402 **DISCUSSION**

403 Furin and TMPRSS2 have both been proposed to process the SARS-CoV-2 spike protein and
404 promote viral entry and infection. In this study, we functionally characterize the role of Furin and
405 TMPRSS2 and show their complementary role in SARS-CoV-2 mechanism of entry and infection.

406 Consistent with previous data (18, 33, 56, 57), processing at S1/S2 is required for optimal viral entry
407 in Calu-3 lung epithelial cells. Indeed, mutation of the arginines of the FCS or blocking S1/S2 cleavage
408 by a series of novel Furin-inhibitors effectively reduced SARS-CoV-2 entry in Calu-3 cells. In the
409 context of cell-to-cell fusion, mutations of the FCS impaired syncytia formation in HeLa cells in the
410 absence of TMPRSS2 in acceptor cells, and Furin-inhibitors phenocopied the effect of these S1/S2
411 mutations. These results highlight the importance of Furin in promoting S-mediated cell-to-cell
412 fusion. In contrast, in HEK293T cells, where SARS-CoV-2 likely enters *via* endocytosis in acidic
413 endosomes, mutations of the FCS enhanced entry (Fig. 6), suggesting that cleavage at S1/S2 by Furin
414 was not required for efficient S-processing by endosomal proteases (e.g., cathepsins) (58, 59). The pH-
415 dependent entry pathway is sensitive to drugs increasing the pH of endosomal compartments, e.g.,
416 hydroxy-chloroquine (47). Nevertheless, this drug failed to show significant improvement in COVID-
417 19 patients (60, 61) or infected animals (62), supporting the notion that the virus can effectively utilize
418 alternative entry pathways that are critical for virus entry, transmission and pathogenicity. The fact that
419 Furin-cleavage at S1/S2 is conserved in SARS-CoV-2 isolated from COVID-19 patients and that
420 ΔPRRA viruses are poorly infectious in hamsters (60), suggest that blocking viral entry through the
421 pH-independent pathway is a viable approach towards thwarting SARS-CoV-2 dissemination. In this
422 context, the non-toxic, small molecules BOS-inhibitors that were analyzed in this study, which can
423 be delivered orally or by inhalation, deserve consideration as potential antivirals against acute
424 SARS-CoV-2 infection. As observed in adult animal models, short-term inhibition of Furin would
425 not cause severe side effects, despite the many physiological functions of this enzyme (20).

426 Our results also demonstrate that Furin can also process S at S2', a site that we map by proteomics
427 to be at **KR**$_{815}$↓SF. The latter S2' cleavage site was confirmed by introducing an optimized S2' site
428 (μS2', KRRKR$_{815}$↓SF) that was efficiently cleaved by Furin, yielding a protein fully competent
429 for fusion in pseudotyped experiments. Importantly, we showed that the S2' processing is strongly
430 increased when ACE2 receptor is expressed. Our results suggest that the recognition of the ACE2
431 receptor by the spîke protein induces a conformational change of the S2 domain and enhances
432 cleavage of S2' site by cellular proteases such as Furin.

433 In contrast TMPRSS2 appears to cleave synthetic peptides encompassing the S1/S2 and S2'
434 cleavage sites and proS protein in Hela cells less efficiently compared to Furin. TMPRSS2 has been
435 reported to enhance the infectivity of SARS-CoV-1 and MERS-CoV *via* cleavages of the S-protein
436 (53, 63), as reviewed in (4, 15, 23). The S1/S2 site VSLL**R**$_{667}$↓ST of SARS-CoV-1 contains an
437 Arg↓Ser cleavage motif that is propitious to cleavage by TMPRSS2 (53) but not by Furin. However,
438 S1 production was minimal and fusion was observed only when donor cells expressing S-protein were
439 co-cultured with acceptor cells expressing ACE2 and TMPRSS2 (53). In SARS-CoV-2 the S1
440 released, presumably following cleavage of S at S1/S2 and ACE2 binding, is much reduced with
441 μS1/S2-S compared to WT-S, indicating that Furin-mediated cleavage at S1/S2 promotes a more
442 efficient release of S1 (Fig. 8B). Additionally, in a co-culture system the relative levels of soluble S1
443 fragment were not affected by the presence or absence of TMPRSS2 for WT and μS1/S2 (Fig. 8B).
444 This suggests that the differential effect of TMPRSS2 on cell-to-cell fusion could not be attributed to
445 its direct cleavage activity on S. Rather, we assert that TMPRSS2 primarily modulates cell-to-cell
446 fusion in part *via* shedding of ACE2. In the presence of TMPRSS2 the extent of fusion would depend
447 on a combination of reduced levels of full-length cell surface ACE2 and increased levels of sACE2
448 that could act as a decoy to inhibit fusion (64). In that context, a human recombinant sACE2 that
449 includes the collectrin domain but lacks the TM domain (hrsACE2, aa 1-740) (see Fig. 10A) effectively

450 blocked SARS-CoV-2 infection of Vero E6 cells (55). Indeed, our cell-to-cell fusion assay tested in
451 co-culture revealed that the ~95 kDa sACE2 primarily produced by TMPRSS2 cleavage of ACE2
452 resulted in lower levels of cellular ACE2 (Figs. 9B, 10B) and in impaired WT-S induced fusion (Figs.
453 9A, 10C). In contrast, the mutant ACE2 (C0+ C4) was no longer sensitive to TMPRSS2 impairment
454 of WT-S-induced fusion, suggesting that the ~80 kDa form of sACE2 primarily produced by
455 TMPRSS2 cleavage of ACE2 (C0+C4), likely upstream of Lys_{619}, may no longer be able to inhibit
456 WT-S-fusion (Fig. 10C), but may still bind S1 as shown by cryoEM studies that used a short ACE2
457 ectodomain (aa 19-615) (40). Altogether, these results suggest that the C-terminal collectrin-like
458 domain (65, 66) of ACE2 (aa 616-768) (Fig. 10A), which is lost in the ~80 kDa form, may be critical
459 for the ability sACE2 to inhibit cell-to-cell fusion of WT-S. Since Arg_{710} and Arg_{716} within the
460 collectrin-like domain (Fig. 10A) have been reported to be implicated in ACE2 dimerization (66), their
461 Ala mutation in the ACE2 (C0+C4) mutant should significantly impair ACE2 dimerization. Whether
462 dimerization of ACE2 and the ~95 kDa sACE2 (Fig. 10B) are needed for efficient inhibition of WT-
463 S-induced fusion (64) is yet to be confirmed.

464 In the context of endogenous expression of ACE2 and TMPRSS2, e.g., in Calu-3 cells (67, 68), our
465 data show that Camostat significantly reduces SARS-CoV-2 infectivity (Fig. 6C), revealing that a
466 TMPRSS2-like activity favors viral entry. Similarly, in the presence of BOS-inhibitors or absence of
467 Furin cleavage at S1/S2, TMPRSS2 enhances cell-to-cell-fusion (Figs. 8A, 9A). HeLa cells expressing
468 WT-S in donor cells and both ACE2 and TMPRSS2 in acceptor cells, exhibited reduced cell-to-cell
469 fusion, a process inhibited by Camostat. This suggests that the relative contribution of TMPRSS2 to
470 the shedding of ACE2 into sACE2 and cleavage of S-protein at S2' is cell-type dependent. Future
471 experiments may unravel the underlying mechanism that would explain the difference between the
472 HeLa and Calu-3 cells. Our study highlights a complex dynamic between spike, ACE2, Furin and
473 TMPRSS2 (Fig. 11) and points to a potential role of TMPRSS2, which in the absence of S1/S2

474 processing (e.g., μAS1/S2 or in presence of BOS-inhibitors) can by shedding ACE2 facilitate S2'
475 cleavage and cell-to-cell fusion.

476 The human airway epithelium is an important site of early SARS-CoV-2 infection (18, 24, 69). The
477 virus can then disseminate to other tissues/cells such as gut, liver, endothelial cells and macrophages
478 where ACE2, Furin and TMPRSS2 are co-expressed (70). While Furin is mostly found in the TGN, it
479 is also present in endosomes and on apical/basolateral plasma membranes in polarized cells such as
480 those of the lung, small intestine and kidney (71). In contrast, TMPRSS2 is mostly found at the apical
481 membrane of secretory epithelia (72), suggesting that both enzymes would be poised to process the S-
482 protein on the apical side. Their relative abundance may be an important factor governing which of the
483 two might cleave S at the S2' cleavage site. The complementarity and interchangeability of these
484 different proteases, together with those in endosomes, likely allows SARS-CoV-2 to exhibit a wider
485 tropism compared to SARS-CoV-1 (73). In this context, we note that randomized placebo controlled
486 clinical trials using an orally administered TMPRSS2 inhibitor Camostat mesilate three times a day for
487 treatment of COVID-19 patients did not show improvement in outcomes (74). We believe that the
488 maximal benefit of TMPRSS2 inhibition could be achieved when Furin activity is also inhibited, since
489 our results showed that TMPRSS2 activity is preponderant in the context of absence of cleavage at
490 S1/S2. Furthermore, the intranasal delivery of both agents would be expected to have less side effects
491 and be more effective, as it would directly target the airway epithelia of the nose and the lungs, the
492 major sites of SARS-CoV-2 entry.

493 Altogether, our results strongly support the notion that a combination of BOS- and selective
494 TMPRSS2-inhibitors would provide a more effective blockade against SARS-CoV-2 infection
495 (Figs. 5D, 11). It would now be interesting to validate *in vivo* whether a combination of a BOS-
496 inhibitor and a more potent/selective TMPRSS2-inhibitor (75) together with hydroxy-chloroquine
497 (56, 76) would synergize the antiviral effect of these entry inhibitors.

498 The availability for worldwide distribution of various SARS-CoV-2 vaccines that inhibit the
499 accessibility of the RBD of S-protein to ACE2 (https://www.raps.org/news-and-articles/news-
500 articles/2020/3/covid-19-vaccine-tracker) represents a major advance to limit the spread of SARS-
501 CoV-2 infections. However, it is still not known with certainty whether they will be effective in
502 patients with impaired immune systems, and whether they will confer a persistent protection
503 against new variants of SARS-CoV-2. If the protective effect of the vaccination remains
504 incomplete, effective antiviral drugs are still needed and could help with early diagnosis of the
505 disease. Ultimately, in case of new emerging coronavirus pandemics (77), the availability of such
506 treatments would constitute a powerful anti-viral arsenal to be used in pandemic preparedness.
507

508 **MATERIALS AND METHODS**

509 **Enzymatic PC-inhibition by BOS-inhibitors**

510 Biochemical assay: The proprotein convertases Furin (108-574-Tev-Flag-6His), PC5A (PCSK5;
511 115-63-Tev-Flag-6His), PACE4 (PCSK6; 150-693-Tev-Flag-6His), and PC7 (PCSK7; 142-634-
512 Tev-Flag-6His) enzymes were purified from BacMam transduced CHO cells. Reactions were
513 performed in black 384-well polystyrene low volume plates (Greiner) at a final volume of 10 µL.
514 BOS-inhibitors (BOS-318, BOS-857 and BOS-981) were dissolved in DMSO (1 mM) and serially
515 diluted 1 to 3 with DMSO through eleven dilutions to provide a final compound concentration
516 range from 0.00017 to 10 µM. 0.05 µl of each concentration was transferred to the corresponding
517 well of an assay plate, and then 5 µl of enzyme (Furin, PCSK5, PCSK6, and PCSK7) in assay
518 buffer (100 mM HEPES pH7.5, 1 mM $CaCl_2$ and 0.005% Triton X-100) was added using a
519 Multidrop Combi (Thermo) to the compound plates to give a final protein concentration of 0.02,
520 0.5, 2.5, and 1.0 nM respectively. The plates were mixed by inversion and following a 30 min
521 preincubation of enzyme with compound at room temperature (~22ºC), the substrate FAM-
522 QRVRRAVGIDK-TAMRA (AnaSpec # 808143, 5 µl of a 1, 0.25, 0.20, and 0.5 µM solution in
523 assay buffer for Furin, PCSK5, PCSK6, and PCSK7 respectively) was added using a Multidrop
524 Combi. The plates were centrifuged at 500 x *g* for 1 minute and incubated at room temperature for
525 two hours. Enzyme inhibition was then quantified using an Envision instrument (PerkinElmer).
526 Data were normalized to maximal inhibition determined by 1 µM decanoyl-Arg-Val-Lys-Arg-
527 chloromethylketone (Calbiochem #344930).

528 Golgi imaging assay: This assay uses an image-based platform to evaluate the intracellular activity
529 of Furin inhibitors. Reactions were performed in black 384-well, tissue culture-treated, clear
530 bottom plates (Greiner). Compounds dissolved in DMSO (1.0 mM) were serially three-fold diluted

531 to give a final compound concentration range from 0.00017 to 10 μM. Analyses were initiated by
532 the addition of U2OS cells simultaneously transduced with a BacMam-delivered construct
533 containing a Golgi-targeting sequence followed by a 12-amino acid Furin/PCSK cleavage site
534 from Bone Morphogenic Protein 10 (BMP10) and then GFP at the C terminus. The dibasic Furin
535 cleavage site sequence was flanked by glycine rich linkers (GalNAc-T2-GGGGS-
536 DSTARIRRNAKG-GGGGS-GFP). Briefly, frozen cells are thawed in assay media (Dulbecco's
537 Modified Eagles Medium Nutritional Mixture F-12 (Ham) without phenol red containing 5% FBS)
538 and diluted to deliver 6000 cells/well (50 μl) to the plate using a Multidrop Combi (Thermo). After
539 a 24-hour incubation period at 37ºC, the cells are stained with Cell Mask Deep Red, fixed in
540 paraformaldehyde and the nuclei stained using Ho33342. The Golgi-targeted GFP forms bright
541 punctate clusters within the cell. In the absence of a Furin/PCSK inhibitor, the endogenous
542 protease cleaves GFP from its N-acetylgalactosaminyltransferase-2 Golgi tether, releasing GFP
543 into the Golgi lumen where fluorescence was diluted below the threshold of assay sensitivity. In
544 the presence of a cell permeable Furin/PCSK inhibitor, GFP fluorescence increases as intra-Golgi
545 protease activity was reduced. Cellular GFP intensity was determined by image-based acquisition
546 (Incell 2200, Perkin Elmer) at 40x magnification with 4 fields measured per well. Multi-scale top
547 hat segmentation was used to identify the GFP-tagged puncta and to quantitate the average
548 fluorescence of all puncta on a per cell basis. Cellular toxicity was determined in parallel.

549 Furin and TMPRSS2 fluorogenic assays: Recombinant Furin was purchased from BioLegend
550 (#719406), human recombinant TRMPSS2 from Cliniscience (ref LS-G57269-100), and the
551 DABCYLGlu-EDANS labelled peptides encompassing the different cleavage sites (SI Table 1)
552 were purchased from Genscript. Reactions were performed at room temperature in black 384-well
553 polystyrene low volume plates (CELLSTAR-Greiner Bio-One # 784476) at a final volume of 15

554 µL. The fluorescent peptides were used at 5 µM and the reactions were performed in 50 mM Tris
555 buffer (pH 6.5 or 7.5), 0.2% Triton X-100, 1mM $CaCl_2$ and Furin was added at a final
556 concentration of 0.2 to 100 nM. BOS-inhibitors (BOS-318, BOS-857 and BOS-981) were
557 dissolved in DMSO (1 mM) and serially diluted 1 to 2 with DMSO to provide a final compound
558 concentration range from 50 µM to 0.01 nM with 5% DMSO in the enzymatic assay. For
559 TMPRSS2, the fluorescent peptides were used at 5 µM and the reactions were performed in 50
560 mM Tris buffer (pH 8), 150 mM NaCl and TMPRSS2 was added at final concentrations of 50 nM.
561 Cleavage of the synthetic peptides was quantitated by determining the increase of EDANS (493
562 nM) fluorescence following release of the DABCYL quencher, which was excited at 335 nM using
563 a Safire 2 Tecan fluorimeter. The fluorescence was followed during 90 min, and the enzymatic
564 activity was deduced by measurement of the increase of fluorescence during the linear phase of
565 the reaction. Each reaction was performed in triplicate and the standard deviation was calculated
566 using Excel-ecart type function ($\sqrt{\frac{\sum(x-\bar{x})^2}{(n-1)}}$).

567 **Plasmids**

568 Single tagged (C-terminal V5 tag) or double tagged (N-terminal HA tag and C-terminal V5 tag)
569 spike-glycoprotein of SARS-CoV-2 (optimized sequence) and its mutants were cloned into the
570 pIRES2-EGFP vector. Site-directed mutagenesis was achieved using a Quick-Change kit
571 (Stratagene, CA) according to the manufacturer's instructions. The plasmids pCI-NEO-hACE2
572 received from DW Lambert (University of Leeds) and pIRES-NEO3-hTMPRSS2 from P Jolicoeur
573 (IRCM). The ΔEnv Vpr Luciferase Reporter Vector (pNL4-3.Luc.R-E-) was obtained from Dr.
574 Nathaniel Landau through the NIH AIDS Reagent Program whereas the pHIV-1NL4-3 ΔEnv-
575 NanoLuc construct was a kind gift from Dr. P Bieniasz. Plasmids encoding VSV-G, as HIV-1
576 Env and tat were previously described (78, 79).

577 **Cell culture and transfection**

578 Monolayers of HeLa, HEK293T, HEK293T17, Vero E6 and Calu-3 cells were cultured in 5% CO_2
579 at 37°C in Dulbecco's modified Eagle's medium (DMEM; Wisent) supplemented with 10% (v/v)
580 fetal bovine serum (FBS; Wisent). HEK293T-ACE2(80), a generous gift from Dr. Paul Bieniasz,
581 were maintained in DMEM containing 10% FBS, 1% nonessential amino acids (NEAA) and 50
582 μg/ml blasticidin (Invivogen). The cells were transfected with JetPrime transfection reagent
583 according to the manufacturer's instructions (Polyplus transfection, New York, USA). At 24h post
584 transfection, the culture media were changed to serum-free and cells incubated for an additional
585 24h. To establish the HeLa cells stably express human ACE2, transfected cells were selected using
586 media containing 500 μg/ml of neomycin (G418, Wisent).

587 For knockdown of Furin in HeLa cells, an optimized set of 4 small interfering RNAs (siRNAs;
588 SMARTPool) targeted against human Furin were purchased from Horizon Discoveries (Perkin
589 Elmer, Lafayette, LA, USA) and transfections of HeLa cells were carried out using INTERFERin
590 (PolyPlus) as recommended by the manufacturer.

591 To generate HIV particles pseudotyped with SARS-CoV-2 S, 293T17 cells (600,000 cells plated
592 in a 6-well vessel) were transfected with 1 μg pNL4-3 Luc.R-E- (or pHIV-1NLΔEnv-NanoLuc)
593 in the presence or absence of 0.3 μg pIR-2019-nCoV-S V5 plasmids using Lipofectamine-3000
594 (Life Technologies). In certain experiments, 293T17 cells were treated with BOS-inhibitors at 6 h
595 post transfection. Pseudovirions expressing the nano- or firefly-luciferase were collected at 24 h
596 or 48 h post transfection, respectively. Viral supernatants were clarified by centrifugation at 300 x
597 *g,* passed through a 0.45-μm pore-size polyvinylidene fluoride (PVDF; Millipore) syringe filter
598 (Millipore; SLGVR33RS), and aliquots frozen at −80°C. For WB analysis of purified
599 pseudovirions, viral supernatants were concentrated by ultracentrifugation on a 20% sucrose

600 cushion for 3h at 35,000 RPM; Beckman Coulter OPTIMA XE; Ti70.1 rotor). HIV particles
601 lacking the SARS-CoV-2 S glycoprotein served as a negative control in all experiments.

602 **Cell viability assay using MTT**

603 Cells, seeded in a 96-well plate, the day before, at 10,000 (HEK-293T and Vero E6) or 50,000
604 (Calu-3) cells, were treated with serial 10-fold dilutions of BOS-inhibitors for up to 48h. Cells
605 treated with vehicle alone were used as negative control. MTT was subsequently added to the
606 medium (final concentration: 2.5 mg/ml) and cells were further incubated for 4h at 37 ^{0}C. After
607 removal of the culture media, DMSO was added and absorbance read at 595 nm using a microplate
608 spectrophotometer. The data from two independent experiments done in triplicates was used to
609 calculate the CC50 by nonlinear regression using GraphPad Prism V5.0 software.

610 **Western blots**

611 The cells were washed with PBS and then lysed using RIPA buffer (1% Triton X-100, 150 mM
612 NaCl, 5 mM EDTA, and 50 mM Tris, pH 7.5) for 30 min at 4ºC. The cell lysates were collected
613 after centrifugation at 14,000 × g for 10 min. The proteins were separated on 7% tris-glycine or
614 8% tricine gels by SDS-PAGE and transferred to a PVDF membrane (Perkin Elmer). The proteins
615 were revealed using a V5-monoclonal antibody (V5-mAb V2660; 1:5000; Invitrogen), ACE2
616 antibody (rabbit monoclonal ab108252; 1:3,000; Abcam), Actin antibody (rabbit polyclonal
617 A2066; 1:5,000; Sigma), or HA-HRP antibody (12-013-819; 1:3,500; Roche). The antigen-
618 antibody complexes were visualized using appropriate HRP conjugated secondary antibodies and
619 enhanced chemiluminescence kit (ECL; Amersham or Bio-Rad) and normalization was reported
620 to β-actin. Quantification of immune-bands was performed using Image Lab software (Bio-Rad).
621 For analysis of SARS-CoV-2 S virions or pseudovirions, protein extracts of purified viral
622 particles and corresponding producing cells (Calu-3 or 293T17, respectively) were resolved on

623 10% tris-glycine gels and immunoblotted for spike, nucleocapsid, HIV-1 Gag p24 or actin using
624 anti-V5 (for pseudovirion detection; V2660)/anti-S2 (for virion detection; Sino Biologicals;
625 40590-T62), anti-N (Sino Biologicals; 40143-MM05), anti-p24 (MBS Hybridoma line 31-90-25)
626 or anti-actin (MP Biomedicals, SKU 08691001), respectively.

627 **Glycosidase treatment**

628 30 to 50 μg proteins were digested for 90 min at 37ºC with endoglycosidase-H (Endo-H; P0702L)
629 or endoglycosidase-F (Endo-F; P0705S) as recommended by the manufacturer (New England
630 Biolabs).

631 **Inhibitor treatment**

632 At 24h post transfection, cells were incubated for 6h with two pan-PC inhibitors: the cell permeable
633 decanoyl-RVKR-chloromethylketone (cmk; 50 mM; 4026850.001; Bachem) or with the cell
634 surface PC-inhibitor hexa-D-arginine (D6R; 20 μM; 344931; EMD). Culture media were then
635 replaced with fresh ones containing the inhibitors for an additional 24h. For the selective cell-
636 permeable Furin-like inhibitors (BOS; Boston Pharmaceuticals), the cells were treated with the
637 inhibitors at the specified concentration starting at 5h pre-transfection and throughout the duration
638 of the experiment.

639 **Cell-to-cell fusion assay**

640 HeLa or HeLa TZM-bl cells were plated at 200,000 cells in 12-well plates. HeLa cells were
641 transiently transfected with different constructs of SARS-CoV-2 spike or NL4.3-HIV Env, or an
642 empty vector and 0.2 μg of CMV-Tat plasmid. HeLa TZM-bl cells were transfected with human
643 ACE2, TMPRSS2 or a combination of both. At 6h post-transfection, media were replaced with
644 fresh ones containing Furin-inhibitors, and 24h later the cells were detached with PBS-EDTA (1
645 μM). Different combinations of HeLa and HeLa-TZM-bl cells were placed in co-culture plate at a

646 ratio of 1:1 for a total of 60,000 cells/well of a 96 well place. After 18-24h the media were removed
647 and 50 µl of cell lysis reagent was added in each well. 20 µl of the cell lysate was used for luciferase
648 reading using 50 µl of Renilla luciferase reagent (Promega, Madison, WI, USA). Relative light
649 units (RLU) were measured using a Promega GLOMAX plate reader (Promega, Madison, WI,
650 USA) and values were reported as fold increase over the RLU measured in co-culture of HeLa
651 cells transfected an empty vector (V) with respective TZM-bl cells.

652 **Protein immunoprecipitation from co-culture media**

653 When indicated, a secreted form of double tagged spike-glycoprotein of SARS-CoV-2 (N-terminal
654 HA tag and C-terminal V5 tag) from media of co-cultured HeLa and HeLa-TZM-bl cells was
655 analyzed by immunoprecipitation. Namely, 0.3 ml of media were precipitated with 25 µl EZ view
656 Red anti-HA affinity gel (E 6779; Sigma-Aldrich) according to the manufacturers' protocol. Upon
657 SDS-PAGE separation and PVDF transfer, the proteins were detected using an HA-HRP antibody
658 (12-013-819; 1:3,500; Roche).

659 **Microscopy**

660 In our luciferase assay, cell co-cultures were plated on glass coverslips. After 18-24h, the cells
661 were incubated with 488 CellMask™ to stain the membrane and then fixed with 4% PFA for 15
662 min at 4ºC. The glass coverslips were mounted on glass slides using ProLong™ Gold Antifade
663 containing DAPI (Invitrogen). The number of syncytia were counted over 10 fields.

664 **Immunofluorescence**

665 Cell culture and transfection were performed on glass coverslips. Cells were washed twice with
666 PBS and fixed with fresh 4% paraformaldehyde for 10 min at room temperature. Following
667 washes, cells were either non-permeabilized or permeabilized with 0.2% Triton X-100 in PBS
668 containing 2% BSA for 5 min, washed, and then blocking was performed with PBS containing 2%

669 BSA for 1h. Cells were incubated with primary antibodies overnight at 4ºC using an antibody
670 against V5 (mouse monoclonal R960-25; 1:1000; Invitrogen), spike (mouse monoclonal
671 GTX632604; 1:500; GeneTex) and ACE2 (goat polyclonal AF933; 1:500; R&D Systems).
672 Following wash, corresponding species-specific Alexa-Fluor (488 or 555)-tagged antibodies
673 (Molecular Probes) were incubated for 1h at room temperature. Coverslips were mounted on a
674 glass slide using ProLong Gold Reagent with DAPI (P36935, Life Technologies). Samples were
675 visualized using a confocal laser-scanning microscope (LSM710, Carl Zeiss) with Plan-
676 Apochromat 63x/1.40 Oil DIC M27 objective on ZEN software.

677 **Pseudovirus entry**

678 HEK293T-ACE2 or Calu-3 (10,000 cells/well plated in a 96-well dish 24 or 48h before,
679 respectively) were incubated with up to 200 µl filtered pseudovirions for overnight. In certain
680 experiments, target cells were pretreated with BOS-318 (1 µM) for 6h and/or Camostat (40 µM)
681 for 2h before transduction. The overnight incubation with pseudovirions was performed in the
682 presence of the inhibitors. Viral inoculum was removed, then fresh media were added, and the
683 cells cultured for up to 72h. Upon removal of spent media, 293T-ACE2 and Calu-3 cells were
684 gently washed twice with PBS and analyzed for firefly- or nano- luciferase activity, respectively
685 using Promega luciferase assay (Cat # E1501) or Nano-Glo luciferase system (Cat # N1110),
686 respectively.

687 **Replication competent SARS-CoV-2 Viruses**

688 SARS-CoV-2, which served as the viral source, was originally isolated from a COVID-19 patient
689 in Quebec, Canada and was designated as LSPQ1. The clinical isolate was amplified, tittered in
690 Vero E6 using a plaque assay as detailed below, and the integrity of the S-protein multi-basic
691 protein convertase site validated by sequencing. All experiments involving infectious SARS-CoV-

692 2 virus were performed in the designated areas of the Biosafety level 3 laboratory (IRCM)
693 previously approved for SARS-CoV-2 work.

694 **Plaque assay in Vero E6 cells**

695 Vero E6 cells (1.2 x 10^5 cells/well) were seeded in quadruplicate in 24-well tissue culture plates in
696 DMEM supplemented with 10% FBS two days before infection. Cells were infected with up to six
697 ten-fold serial dilutions (10^{-2}-10^{-6}) of viral supernatant containing SARS-CoV-2 for 1h at 37ºC
698 (200 µl infection volume). The plates were manually rocked every 15 min during the 1-hour period.
699 Subsequently, virus was removed, cells were washed and overlaying media (containing 0.6% low
700 melt agarose in DMEM with 10% FBS) was added and incubated undisturbed for 60-65h at 37ºC.
701 Post incubation, cells were fixed with 4% formaldehyde and stained with 0.25% crystal violet
702 (prepared in 30% methanol). High quality plaque pictures were taken using a high resolution
703 DLSR camera (Nikon model: D80, objective: "AF Micro-Nikkor 60mm f/2.8D"). Plaques were
704 counted manually and in parallel, imaged plaque plates were processed and plaques enumerated
705 using an automated algorithm based Matlab software. Virus titer is expressed as plaque-forming
706 units per ml (PFU/ml): (number of plaques x dilution factor of the virus) x 1000 / volume of virus
707 dilution used for infection (in µl). Multiplicity of infection (MOI) expressed as: MOI = PFU of
708 virus used for infection / number of cells.

709 **Cell infections with fully replicative SARS-CoV-2**

710 Vero E.6 and Calu-3 cells were seeded in duplicates in 12-well plates (2.3 x 10^5 cells/well) the day
711 before. Cells were pre-treated with various concentrations (0.1-1µM) of BOS-inhibitors and
712 vehicle alone (DMSO) for up to 24h. In certain experiments, Calu-3 were also pre-treated with
713 Camostat for 1h. Thereafter, the cells were infected with SARS-CoV-2 virus at MOI of 0.001 for
714 1h (Vero E6) or 0.01 for 3h (Calu-3 cells) in 350 µl of serum-free DMEM at 37ºC with occasional

715 manual rocking of plates. Cells plus media only were used as a control. After incubation, virus
716 was removed, and the cell monolayer was washed twice successively with PBS and serum-free
717 DMEM. New media (total 1ml) containing the concentrations of BOS-inhibitors was subsequently
718 added to cells. Cell-free supernatant (250 µl) was removed at 12, 24 and 48h post infection. The
719 drugs were replenished for 1 ml media at 24h post-infection. The virus supernatants were stored
720 at -80°C until further use. Viral production in the supernatant was quantified using a plaque assay
721 on Vero E6.1 cells as described above. In certain experiments, viral supernatants were harvested
722 at the end of infection and purified on a 20% sucrose cushion using ultracentrifugation as described
723 above. The resulting concentrated virus and corresponding infected cells were analyzed by
724 Western blotting as appropriate.

725 Quantification and statistical analysis: Virus titers quantified by plaque assay in triplicate were
726 shown as mean ± standard deviation. The results from experiments done with two biological
727 replicates and two technical replicates in triplicates were used to calculate the IC_{50} by nonlinear
728 regression using GraphPad Prism V5.0 software. The difference between the control cells (virus
729 with 0.001% DMSO) and the cells treated with BOS-inhibitors were evaluated by Student's t test.
730 The P values of 0.05 or lower were considered statistically significant (*, $p < 0.05$; **, $p < 0.01$;
731 ***, $p < 0.001$).

732

733 **DATA AVAILABILITY**

734 Source data are provided with this paper. The data that support the findings of this study are
735 preserved at repositories of the Montreal Clinical Research Institute (IRCM), Montreal, QC,
736 Canada and available from the corresponding authors upon reasonable request.

737

738 **ACKNOWLEDGEMENTS**

739 This work was supported in part by CIHR Foundation grants (NGS: # 148363) and (ÉAC: #
740 154324), a Canada Research Chairs in Precursor Proteolysis (NGS: # 950-231335), a CIHR
741 CHAMPS Team Grant # HAL 157986 (NGS and ÉAC), Réseau SIDA maladies infectieuses
742 COVID-19 initiative (ÉAC and NGS), the European score project and ANR Reacting COVID-19
743 (ED and BC). The authors thank the Quebec public health laboratory for providing the infectious
744 isolate LSPQ1 SARS-CoV-2. We thank Paul Bieniasz for the 293T-ACE2 cell line and the pHIV-
745 1NL4-3ΔEnv-NanoLuc construct. The following reagents were obtained from the NIH AIDS
746 Reagent Program, Division of AIDS, NIAID, NIH: TZM-bl cells, from John C. Kappes, Xiaoyun
747 Wu, and Tranzyme, Inc. and HIV-1 pNL4-3 ΔEnv Vpr Luciferase Reporter Vector (pNL4-
748 3.Luc.R-E-) obtained from Nathaniel Landau. We are thankful to Dominic Filion for developing
749 the algorithm for image-assisted plaque quantification. JJ is supported by the CIHR Postdoctoral
750 Fellowship (HIV-435243-73284). We also thank Dr Annik Prat (IRCM) for the design of the
751 summary model shown in Fig. 7. Finally, we would like to thank Mrs. Habiba Oueslati and Brigitte
752 Mary for ther excellent editorial help and organization of the manuscript.

753 **AUTHOR CONTRIBUTIONS**

754 RE made all the original critical experiments revealing the role of the PCs in spike processing and
755 the effect of their inhibitors. JJ performed all the cell assays with infectious SARS-CoV-2. DSR
756 participated in the biochemical characterizations of TMPRSS2 processing of ACE2 and S1. UA
757 performed all cell-to-cell fusion assays. AE made all the mutants used in the work. RMD generated
758 the HeLa-ACE2 cells and prepared all the cells for *ex vivo* analyses. DNH performed all the
759 immunocytochemical experiments. FD and ML performed experiments related to SARS-CoV-2
760 pseudovirions. AD and PSO performed all the Furin and TMPRSS2 *in vitro* kinetic cleavage
761 analyses of peptides mimicking the S1/S2 and S2' sites. CM and KW provided the BOS-inhibitors

762 and their characterization. ED made seminal contributions to the possible role of Furin-like
763 enzymes in the processing of the spike-glycoprotein and actively contributed to the
764 conceptualization and writing of the manuscript. TNQP designed, performed, and analyzed
765 experiments related to viral entry and contributed to the writing of the manuscript. EAC (virology)
766 and NGS (biochemistry and cell biology) conceptualized the research program and provided the
767 intellectual contributions and funding for the whole project. All authors actively contributed to the
768 final version of the manuscript.

769

770 **REFERENCES**

771

772 1. Dobson AP, Carper ER. 1996. Infectious Diseases and Human Population History:
773 Throughout history the establishment of disease has been a side effect of the growth of
774 civilization. Bioscience 46:115-126.

775 2. Cui J, Li F, Shi ZL. 2019. Origin and evolution of pathogenic coronaviruses. Nat Rev
776 Microbiol 17:181-192.

777 3. Almeida JD, Tyrrell DA. 1967. The morphology of three previously uncharacterized
778 human respiratory viruses that grow in organ culture. J Gen Virol 1:175-8.

779 4. Belouzard S, Millet JK, Licitra BN, Whittaker GR. 2012. Mechanisms of coronavirus cell
780 entry mediated by the viral spike protein. Viruses 4:1011-33.

781 5. Liu PP, Blet A, Smyth D, Li H. 2020. The Science Underlying COVID-19: Implications
782 for the Cardiovascular System. Circulation 142:68-78.

783 6. Usul Afsar C. 2020. 2019-nCoV-SARS-CoV-2 (COVID-19) infection: Crucıalıty of Furın
784 and relevance wıth cancer. Med Hypotheses 140:109770.

785 7. Braun E, Sauter D. 2019. Furin-mediated protein processing in infectious diseases and
786 cancer. Clin Transl Immunology 8:e1073.

787 8. Izaguirre G. 2019. The Proteolytic Regulation of Virus Cell Entry by Furin and Other
788 Proprotein Convertases. Viruses 11.

789 9. Seidah NG, Pasquato A, Andreo U. 2021. How Do Enveloped Viruses Exploit the
790 Secretory Proprotein Convertases to Regulate Infectivity and Spread? Viruses 13:1229.

791 10. Coutard B, Valle C, de Lamballerie X, Canard B, Seidah NG, Decroly E. 2020. The spike
792 glycoprotein of the new coronavirus 2019-nCoV contains a furin-like cleavage site absent
793 in CoV of the same clade. Antiviral Res 176:104742.

794 11. Tang T, Bidon M, Jaimes JA, Whittaker GR, Daniel S. 2020. Coronavirus membrane
795 fusion mechanism offers as a potential target for antiviral development. Antiviral Res
796 doi:10.1016/j.antiviral.2020.104792:104792.
797 12. Hoffmann M, Kleine-Weber H, Pöhlmann S. 2020. A Multibasic Cleavage Site in the Spike
798 Protein of SARS-CoV-2 Is Essential for Infection of Human Lung Cells. Mol Cell 78:779-
799 784.e5.
800 13. Lan J, Ge J, Yu J, Shan S, Zhou H, Fan S, Zhang Q, Shi X, Wang Q, Zhang L, Wang X.
801 2020. Structure of the SARS-CoV-2 spike receptor-binding domain bound to the ACE2
802 receptor. Nature 581:215-220.
803 14. Lu G, Wang Q, Gao GF. 2015. Bat-to-human: spike features determining 'host jump' of
804 coronaviruses SARS-CoV, MERS-CoV, and beyond. Trends Microbiol 23:468-78.
805 15. Millet JK, Whittaker GR. 2018. Physiological and molecular triggers for SARS-CoV
806 membrane fusion and entry into host cells. Virology 517:3-8.
807 16. Ou X, Liu Y, Lei X, Li P, Mi D, Ren L, Guo L, Guo R, Chen T, Hu J, Xiang Z, Mu Z,
808 Chen X, Chen J, Hu K, Jin Q, Wang J, Qian Z. 2020. Characterization of spike glycoprotein
809 of SARS-CoV-2 on virus entry and its immune cross-reactivity with SARS-CoV. Nat
810 Commun 11:1620.
811 17. Shang J, Wan Y, Luo C, Ye G, Geng Q, Auerbach A, Li F. 2020. Cell entry mechanisms
812 of SARS-CoV-2. Proc Natl Acad Sci U S A 117:11727-11734.
813 18. Bestle D, Heindl MR, Limburg H, Van Lam van T, Pilgram O, Moulton H, Stein DA,
814 Hardes K, Eickmann M, Dolnik O, Rohde C, Klenk HD, Garten W, Steinmetzer T,
815 Böttcher-Friebertshäuser E. 2020. TMPRSS2 and furin are both essential for proteolytic
816 activation of SARS-CoV-2 in human airway cells. Life Sci Alliance 3.

817 19. Mykytyn AZ, Breugem TI, Riesebosch S, Schipper D, van den Doel PB, Rottier RJ,
818 Lamers MM, Haagmans BL. 2021. SARS-CoV-2 entry into human airway organoids is
819 serine protease-mediated and facilitated by the multibasic cleavage site. Elife 10.
820 20. Seidah NG, Prat A. 2012. The biology and therapeutic targeting of the proprotein
821 convertases. Nat Rev Drug Discov 11:367-383.
822 21. Van de Ven WJ, Creemers JW, Roebroek AJ. 1991. Furin: the prototype mammalian
823 subtilisin-like proprotein-processing enzyme. Endoproteolytic cleavage at paired basic
824 residues of proproteins of the eukaryotic secretory pathway. Enzyme 45:257-270.
825 22. Moulard M, Decroly E. 2000. Maturation of HIV envelope glycoprotein precursors by
826 cellular endoproteases. Biochim Biophys Acta 1469:121-132.
827 23. Millet JK, Whittaker GR. 2015. Host cell proteases: Critical determinants of coronavirus
828 tropism and pathogenesis. Virus Res 202:120-34.
829 24. Hoffmann M, Kleine-Weber H, Schroeder S, Kruger N, Herrler T, Erichsen S, Schiergens
830 TS, Herrler G, Wu NH, Nitsche A, Muller MA, Drosten C, Pohlmann S. 2020. SARS-
831 CoV-2 Cell Entry Depends on ACE2 and TMPRSS2 and Is Blocked by a Clinically Proven
832 Protease Inhibitor. Cell 181:271-280.e8.
833 25. Xia S, Lan Q, Su S, Wang X, Xu W, Liu Z, Zhu Y, Wang Q, Lu L, Jiang S. 2020. The role
834 of furin cleavage site in SARS-CoV-2 spike protein-mediated membrane fusion in the
835 presence or absence of trypsin. Signal Transduct Target Ther 5:92.
836 26. Johnson BA, Xie X, Bailey AL, Kalveram B, Lokugamage KG, Muruato A, Zou J, Zhang
837 X, Juelich T, Smith JK, Zhang L, Bopp N, Schindewolf C, Vu M, Vanderheiden A, Winkler
838 ES, Swetnam D, Plante JA, Aguilar P, Plante KS, Popov V, Lee B, Weaver SC, Suthar
839 MS, Routh AL, Ren P, Ku Z, An Z, Debbink K, Diamond MS, Shi PY, Freiberg AN,

840 Menachery VD. 2021. Loss of furin cleavage site attenuates SARS-CoV-2 pathogenesis.
841 Nature doi:10.1038/s41586-021-03237-4.
842 27. Peacock TP, Goldhill DH, Zhou J, Baillon L, Frise R, Swann OC, Kugathasan R, Penn R,
843 Brown JC, Sanchez-David RY, Braga L, Williamson MK, Hassard JA, Staller E, Hanley
844 B, Osborn M, Giacca M, Davidson AD, Matthews DA, Barclay WS. 2021. The furin
845 cleavage site in the SARS-CoV-2 spike protein is required for transmission in ferrets. Nat
846 Microbiol doi:10.1038/s41564-021-00908-w.
847 28. Johnson BA, Xie X, Bailey AL, Kalveram B, Lokugamage KG, Muruato A, Zou J, Zhang
848 X, Juelich T, Smith JK, Zhang L, Bopp N, Schindewolf C, Vu M, Vanderheiden A, Winkler
849 ES, Swetnam D, Plante JA, Aguilar P, Plante KS, Popov V, Lee B, Weaver SC, Suthar
850 MS, Routh AL, Ren P, Ku Z, An Z, Debbink K, Diamond MS, Shi PY, Freiberg AN,
851 Menachery VD. 2021. Loss of furin cleavage site attenuates SARS-CoV-2 pathogenesis.
852 Nature 591:293-299.
853 29. Afar DE, Vivanco I, Hubert RS, Kuo J, Chen E, Saffran DC, Raitano AB, Jakobovits A.
854 2001. Catalytic cleavage of the androgen-regulated TMPRSS2 protease results in its
855 secretion by prostate and prostate cancer epithelia. Cancer Res 61:1686-92.
856 30. Shrimp JH, Kales SC, Sanderson PE, Simeonov A, Shen M, Hall MD. 2020. An Enzymatic
857 TMPRSS2 Assay for Assessment of Clinical Candidates and Discovery of Inhibitors as
858 Potential Treatment of COVID-19. bioRxiv doi:10.1101/2020.06.23.167544.
859 31. Kawase M, Shirato K, van der Hoek L, Taguchi F, Matsuyama S. 2012. Simultaneous
860 treatment of human bronchial epithelial cells with serine and cysteine protease inhibitors
861 prevents severe acute respiratory syndrome coronavirus entry. J Virol 86:6537-45.

862 32. Nimishakavi S, Raymond WW, Gruenert DC, Caughey GH. 2015. Divergent Inhibitor
863 Susceptibility among Airway Lumen-Accessible Tryptic Proteases. PLoS One
864 10:e0141169.
865 33. Hörnich BF, Großkopf AK, Schlagowski S, Tenbusch M, Kleine-Weber H, Neipel F,
866 Stahl-Hennig C, Hahn AS. 2021. SARS-CoV-2 and SARS-CoV spike-mediated cell-cell
867 fusion differ in the requirements for receptor expression and proteolytic activation. J Virol
868 doi:10.1128/jvi.00002-21.
869 34. Cyranoski D. 2020. Profile of a killer: the complex biology powering the coronavirus
870 pandemic. Nature 581:22-26.
871 35. Matoba Y, Aoki Y, Tanaka S, Yahagi K, Katsushima Y, Katsushima F, Sugawara K,
872 Matsuzaki Y, Mizuta K. 2016. HeLa-ACE2-TMPRSS2 Cells Are Useful for the Isolation
873 of Human Coronavirus 229E. Jpn J Infect Dis 69:452-4.
874 36. Thomas G. 2002. Furin at the cutting edge: from protein traffic to embryogenesis and
875 disease. Nature Reviews Molecular Cell Biology 3:753-766.
876 37. Örd M, Faustova I, Loog M. 2020. Biochemical evidence of furin specificity and potential
877 for phospho-regulation at Spike protein S1/S2 cleavage site in SARS-CoV2 but not in
878 SARS-CoV1 or MERS-CoV. bioRxiv
879 doi:10.1101/2020.06.23.166900:2020.06.23.166900.
880 38. Andersen KG, Rambaut A, Lipkin WI, Holmes EC, Garry RF. 2020. The proximal origin
881 of SARS-CoV-2. Nat Med 26:450-452.
882 39. Schjoldager KT, Clausen H. 2012. Site-specific protein O-glycosylation modulates
883 proprotein processing - deciphering specific functions of the large polypeptide GalNAc-
884 transferase gene family. Biochim Biophys Acta 1820:2079-2094.

885 40. Benton DJ, Wrobel AG, Xu P, Roustan C, Martin SR, Rosenthal PB, Skehel JJ, Gamblin
886 SJ. 2020. Receptor binding and priming of the spike protein of SARS-CoV-2 for membrane
887 fusion. Nature 588:327-330.
888 41. Belouzard S, Chu VC, Whittaker GR. 2009. Activation of the SARS coronavirus spike
889 protein via sequential proteolytic cleavage at two distinct sites. Proc Natl Acad Sci U S A
890 106:5871-6.
891 42. Hallenberger S, Bosch V, Angliker H, Shaw E, Klenk HD, Garten W. 1992. Inhibition of
892 furin-mediated cleavage activation of HIV-1 glycoprotein gp160. Nature 360:358-361.
893 43. Susan-Resiga D, Essalmani R, Hamelin J, Asselin MC, Benjannet S, Chamberland A, Day
894 R, Szumska D, Constam D, Bhattacharya S, Prat A, Seidah NG. 2011. Furin Is the Major
895 Processing Enzyme of the Cardiac-specific Growth Factor Bone Morphogenetic Protein
896 10. J Biol Chem 286:22785-22794.
897 44. Cheng YW, Chao TL, Li CL, Chiu MF, Kao HC, Wang SH, Pang YH, Lin CH, Tsai YM,
898 Lee WH, Tao MH, Ho TC, Wu PY, Jang LT, Chen PJ, Chang SY, Yeh SH. 2020. Furin
899 Inhibitors Block SARS-CoV-2 Spike Protein Cleavage to Suppress Virus Production and
900 Cytopathic Effects. Cell Rep 33:108254.
901 45. Walls AC, Park YJ, Tortorici MA, Wall A, McGuire AT, Veesler D. 2020. Structure,
902 Function, and Antigenicity of the SARS-CoV-2 Spike Glycoprotein. Cell 181:281-292.e6.
903 46. Hoffmann M, Mösbauer K, Hofmann-Winkler H, Kaul A, Kleine-Weber H, Krüger N,
904 Gassen NC, Müller MA, Drosten C, Pöhlmann S. 2020. Chloroquine does not inhibit
905 infection of human lung cells with SARS-CoV-2. Nature 585:588-590.
906 47. Vincent MJ, Bergeron E, Benjannet S, Erickson BR, Rollin PE, Ksiazek TG, Seidah NG,
907 Nichol ST. 2005. Chloroquine is a potent inhibitor of SARS coronavirus infection and
908 spread. Virol J 2:69.

909 48. Bayati A, Kumar R, Francis V, McPherson PS. 2021. SARS-CoV-2 infects cells following
910 viral entry via clathrin-mediated endocytosis. J Biol Chem 296:100306.
911 49. Platt EJ, Wehrly K, Kuhmann SE, Chesebro B, Kabat D. 1998. Effects of CCR5 and CD4
912 cell surface concentrations on infections by macrophagetropic isolates of human
913 immunodeficiency virus type 1. J Virol 72:2855-64.
914 50. Plante JA, Mitchell BM, Plante KS, Debbink K, Weaver SC, Menachery VD. 2021. The
915 variant gambit: COVID-19's next move. Cell Host Microbe 29:508-515.
916 51. Peacock TP, Penrice-Randal R, Hiscox JA, Barclay WS. 2021. SARS-CoV-2 one year on:
917 evidence for ongoing viral adaptation. J Gen Virol 102.
918 52. Rajah MM, Hubert M, Bishop E, Saunders N, Robinot R, Grzelak L, Planas D, Dufloo J,
919 Gellenoncourt S, Bongers A, Zivaljic M, Planchais C, Guivel-Benhassine F, Porrot F,
920 Mouquet H, Chakrabarti LA, Buchrieser J, Schwartz O. 2021. SARS-CoV-2 Alpha, Beta,
921 and Delta variants display enhanced Spike-mediated syncytia formation. EMBO J
922 doi:10.15252/embj.2021108944:e108944.
923 53. Matsuyama S, Nagata N, Shirato K, Kawase M, Takeda M, Taguchi F. 2010. Efficient
924 activation of the severe acute respiratory syndrome coronavirus spike protein by the
925 transmembrane protease TMPRSS2. J Virol 84:12658-64.
926 54. Heurich A, Hofmann-Winkler H, Gierer S, Liepold T, Jahn O, Pöhlmann S. 2014.
927 TMPRSS2 and ADAM17 cleave ACE2 differentially and only proteolysis by TMPRSS2
928 augments entry driven by the severe acute respiratory syndrome coronavirus spike protein.
929 J Virol 88:1293-307.
930 55. Monteil V, Kwon H, Prado P, Hagelkrüys A, Wimmer RA, Stahl M, Leopoldi A, Garreta
931 E, Hurtado Del Pozo C, Prosper F, Romero JP, Wirnsberger G, Zhang H, Slutsky AS,
932 Conder R, Montserrat N, Mirazimi A, Penninger JM. 2020. Inhibition of SARS-CoV-2

933 Infections in Engineered Human Tissues Using Clinical-Grade Soluble Human ACE2. Cell
934 181:905-913.e7.
935 56. Hoffmann M, Mösbauer K, Hofmann-Winkler H, Kaul A, Kleine-Weber H, Krüger N,
936 Gassen NC, Müller MA, Drosten C, Pöhlmann S. 2020. Chloroquine does not inhibit
937 infection of human lung cells with SARS-CoV-2. Nature doi:10.1038/s41586-020-2575-3.
938 57. Bellamine A, Pham TNQ, Jain J, Wilson J, Sahin K, Dallaire F, Seidah NG, Durkee S,
939 Radošević K, Cohen É A. 2021. L-Carnitine Tartrate Downregulates the ACE2 Receptor
940 and Limits SARS-CoV-2 Infection. Nutrients 13.
941 58. Padmanabhan P, Desikan R, Dixit NM. 2020. Targeting TMPRSS2 and Cathepsin B/L
942 together may be synergistic against SARS-CoV-2 infection. PLoS Comput Biol
943 16:e1008461.
944 59. Papa G, Mallery DL, Albecka A, Welch LG, Cattin-Ortolá J, Luptak J, Paul D, McMahon
945 HT, Goodfellow IG, Carter A, Munro S, James LC. 2021. Furin cleavage of SARS-CoV-
946 2 Spike promotes but is not essential for infection and cell-cell fusion. PLoS Pathog
947 17:e1009246.
948 60. Altulea D, Maassen S, Baranov MV, van den Bogaart G. 2021. What makes
949 (hydroxy)chloroquine ineffective against COVID-19: insights from cell biology. J Mol
950 Cell Biol doi:10.1093/jmcb/mjab016.
951 61. Self WH, Semler MW, Leither LM, Casey JD, Angus DC, Brower RG, Chang SY, Collins
952 SP, Eppensteiner JC, Filbin MR, Files DC, Gibbs KW, Ginde AA, Gong MN, Harrell FE,
953 Jr, Hayden DL, Hough CL, Johnson NJ, Khan A, Lindsell CJ, Matthay MA, Moss M, Park
954 PK, Rice TW, Robinson BRH, Schoenfeld DA, Shapiro NI, Steingrub JS, Ulysse CA,
955 Weissman A, Yealy DM, Thompson BT, Brown SM, National Heart L, Network BIPCT.

956 2020. Effect of Hydroxychloroquine on Clinical Status at 14 Days in Hospitalized Patients
957 With COVID-19: A Randomized Clinical Trial. JAMA 324:2165-2176.
958 62. Rosenke K, Jarvis MA, Feldmann F, Schwarz B, Okumura A, Lovaglio J, Saturday G,
959 Hanley PW, Meade-White K, Williamson BN, Hansen F, Perez-Perez L, Leventhal S,
960 Tang-Huau TL, Callison J, Haddock E, Stromberg KA, Scott D, Sewell G, Bosio CM,
961 Hawman D, de Wit E, Feldmann H. 2020. Hydroxychloroquine prophylaxis and treatment
962 is ineffective in macaque and hamster SARS-CoV-2 disease models. JCI Insight 5.
963 63. Glowacka I, Bertram S, Müller MA, Allen P, Soilleux E, Pfefferle S, Steffen I, Tsegaye
964 TS, He Y, Gnirss K, Niemeyer D, Schneider H, Drosten C, Pöhlmann S. 2011. Evidence
965 that TMPRSS2 activates the severe acute respiratory syndrome coronavirus spike protein
966 for membrane fusion and reduces viral control by the humoral immune response. J Virol
967 85:4122-34.
968 64. Raghuvamsi PV, Tulsian NK, Samsudin F, Qian X, Purushotorman K, Yue G, Kozma MM,
969 Hwa WY, Lescar J, Bond PJ, MacAry PA, Anand GS. 2021. SARS-CoV-2 S protein:ACE2
970 interaction reveals novel allosteric targets. Elife 10.
971 65. Zhang H, Wada J, Hida K, Tsuchiyama Y, Hiragushi K, Shikata K, Wang H, Lin S, Kanwar
972 YS, Makino H. 2001. Collectrin, a collecting duct-specific transmembrane glycoprotein, is
973 a novel homolog of ACE2 and is developmentally regulated in embryonic kidneys. J Biol
974 Chem 276:17132-9.
975 66. Yan R, Zhang Y, Li Y, Xia L, Guo Y, Zhou Q. 2020. Structural basis for the recognition
976 of SARS-CoV-2 by full-length human ACE2. Science 367:1444-1448.
977 67. Yamamoto M, Kiso M, Sakai-Tagawa Y, Iwatsuki-Horimoto K, Imai M, Takeda M,
978 Kinoshita N, Ohmagari N, Gohda J, Semba K, Matsuda Z, Kawaguchi Y, Kawaoka Y,
979 Inoue JI. 2020. The Anticoagulant Nafamostat Potently Inhibits SARS-CoV-2 S Protein-

980 Mediated Fusion in a Cell Fusion Assay System and Viral Infection In Vitro in a Cell-
981 Type-Dependent Manner. Viruses 12.
982 68. Koch J, Uckeley ZM, Doldan P, Stanifer M, Boulant S, Lozach PY. 2021. TMPRSS2
983 expression dictates the entry route used by SARS-CoV-2 to infect host cells. EMBO J
984 40:e107821.
985 69. Wölfel R, Corman VM, Guggemos W, Seilmaier M, Zange S, Müller MA, Niemeyer D,
986 Jones TC, Vollmar P, Rothe C, Hoelscher M, Bleicker T, Brünink S, Schneider J, Ehmann
987 R, Zwirglmaier K, Drosten C, Wendtner C. 2020. Virological assessment of hospitalized
988 patients with COVID-2019. Nature 581:465-469.
989 70. Zhou L, Niu Z, Jiang X, Zhang Z, Zheng Y, Wang Z, Zhu Y, Gao L, Huang H, Wang X,
990 Sun Q. 2020. The SARS-CoV-2 targets by the pscRNA profiling of ACE2, TMPRSS2 and
991 Furin proteases. iScience doi:10.1016/j.isci.2020.101744:101744.
992 71. Mayer G, Boileau G, Bendayan M. 2004. Sorting of furin in polarized epithelial and
993 endothelial cells: expression beyond the Golgi apparatus. J Histochem Cytochem 52:567-
994 580.
995 72. Antalis TM, Bugge TH, Wu Q. 2011. Membrane-anchored serine proteases in health and
996 disease. Prog Mol Biol Transl Sci 99:1-50.
997 73. Chu H, Chan JF, Yuen TT, Shuai H, Yuan S, Wang Y, Hu B, Yip CC, Tsang JO, Huang
998 X, Chai Y, Yang D, Hou Y, Chik KK, Zhang X, Fung AY, Tsoi HW, Cai JP, Chan WM,
999 Ip JD, Chu AW, Zhou J, Lung DC, Kok KH, To KK, Tsang OT, Chan KH, Yuen KY.
1000 2020. Comparative tropism, replication kinetics, and cell damage profiling of SARS-CoV-
1001 2 and SARS-CoV with implications for clinical manifestations, transmissibility, and
1002 laboratory studies of COVID-19: an observational study. Lancet Microbe 1:e14-e23.

1003 74. Gunst JD, Staerke NB, Pahus MH, Kristensen LH, Bodilsen J, Lohse N, Dalgaard LS,
1004 Brønnum D, Fröbert O, Hønge B, Johansen IS, Monrad I, Erikstrup C, Rosendal R, Vilstrup
1005 E, Mariager T, Bove DG, Offersen R, Shakar S, Cajander S, Jørgensen NP, Sritharan SS,
1006 Breining P, Jespersen S, Mortensen KL, Jensen ML, Kolte L, Frattari GS, Larsen CS,
1007 Storgaard M, Nielsen LP, Tolstrup M, Sædder EA, Østergaard LJ, Ngo HTT, Jensen MH,
1008 Højen JF, Kjolby M, Søgaard OS. 2021. Efficacy of the TMPRSS2 inhibitor camostat
1009 mesilate in patients hospitalized with Covid-19-a double-blind randomized controlled trial.
1010 EClinicalMedicine 35:100849.
1011 75. Shapira T, Monreal IA, Dion SP, Jager M, Désilets A, Olmstead AD, Vandal T, Buchholz
1012 DW, Imbiakha B, Gao G, Chin A, Rees WD, Steiner T, Nabi IR, Marsault E, Sahler J,
1013 August A, Van de Walle G, Whittaker GR, Boudreault PL, Aguilar HC, Leduc R, Jean F.
1014 2021. A novel highly potent inhibitor of TMPRSS2-like proteases blocks SARS-CoV-2
1015 variants of concern and is broadly protective against infection and mortality in mice.
1016 bioRxiv doi:10.1101/2021.05.03.442520.
1017 76. Ou T, Mou H, Zhang L, Ojha A, Choe H, Farzan M. 2021. Hydroxychloroquine-mediated
1018 inhibition of SARS-CoV-2 entry is attenuated by TMPRSS2. PLoS Pathog 17:e1009212.
1019 77. Morens DM, Fauci AS. 2020. Emerging Pandemic Diseases: How We Got to COVID-19.
1020 Cell 183:837.
1021 78. Lodge R, Lalonde JP, Lemay G, Cohen EA. 1997. The membrane-proximal
1022 intracytoplasmic tyrosine residue of HIV-1 envelope glycoprotein is critical for basolateral
1023 targeting of viral budding in MDCK cells. EMBO J 16:695-705.
1024 79. Forget J, Yao XJ, Mercier J, Cohen EA. 1998. Human immunodeficiency virus type 1 vpr
1025 protein transactivation function: mechanism and identification of domains involved. J Mol
1026 Biol 284:915-23.

1027 80. Schmidt F, Weisblum Y, Muecksch F, Hoffmann HH, Michailidis E, Lorenzi JCC,
1028 Mendoza P, Rutkowska M, Bednarski E, Gaebler C, Agudelo M, Cho A, Wang Z,
1029 Gazumyan A, Cipolla M, Caskey M, Robbiani DF, Nussenzweig MC, Rice CM,
1030 Hatziioannou T, Bieniasz PD. 2020. Measuring SARS-CoV-2 neutralizing antibody
1031 activity using pseudotyped and chimeric viruses. J Exp Med 217.

1032

1033

1034 **FIGURE LEGENDS**

1035 Figure 1: **Processing of S-peptides by Furin and TMPRSS2. (A)** Schematic representation of
1036 the primary structure of preproS and its domains and the predicted Furin-like S1/S2 site generating
1037 the S1- and S2-subunits, as well as the S2' site preceding the fusion peptide (FP). The signal
1038 peptide (SP), N-terminal domain (NTD), receptor binding domain (RBD) to ACE2, the two heptad
1039 repeats HR1 and HR2, the transmembrane domain (TM), the cytosolic tail (CT) and the C-terminal
1040 V5-tag are indicated. **(B)** *In vitro* Furin activity against peptides mimicking the S1/S2 (and its
1041 mutants) and S2' cleavage site sequence of the spike protein from SARS-CoV-2 and SARS-CoV-
1042 1, as described in SI-Table 1. Each substrate was tested at a final protease concentration of 2 and
1043 100 nM. **(C)** *In vitro* TMPRSS2 activity (at 50 nM) against peptides mimicking the S1/S2 and S2'
1044 cleavage site sequence of the spike protein from SARS-CoV-2 (and its mutants) described in SI-
1045 Table 1.

1046 Figure 2: **Processing of spike-glycoprotein in HeLa cells.** (**A**) Western blot analyses of the
1047 processing of WT proS into V5-tagged S2 and S2' by the proprotein convertases Furin, PC5A,
1048 PACE4 and PC7 following co-transfection of their cDNAs in HeLa cells. The migration positions
1049 of immature $proS_{im}$, S2 and S2' as well as the actin loading control are emphasized. V = empty
1050 pIRES-EGFP-V5 vector. (**B**) Western blot analyses of HeLa cells following co-transfection with
1051 cDNAs coding for either WT-S-protein or its double Ala-mutant [R685A + R682A] (μS1/S2) in the
1052 absence or presence of Furin cDNA at a ratio S:protease = 1:2. *Inconsistently observed oligomeric
1053 forms of proS. (**C**) Identification of S2' cleavage site by MS/MS. WT-spike-glycoprotein was
1054 immunoprecipitated from HeLa cells using V5 agarose beads then resolved by SDS
1055 electrophoresis SDS/PAGE and subjected to silver staining (left panel); the positions of the slices
1056 are indicated (1 to 10). The MS/MS analysis of peptides generated by a Lys-specific protease

1057 (K_{814}↓) are indicated; the data represent the ratio of SFIEDLLFNK825 to $\underline{R}_{815}$SFIEDLLFN$\underline{K}_{825}$
1058 (right panel). (**D**) Western blot analyses of HeLa cells co-transfected with V5-tagged spike protein,
1059 WT (S) or its Furin-optimized S2' (K<u>RR</u>KR_{815}↓SF) mutant (μS2'), and empty vector (V) or Furin.
1060 (**A, B**) The estimated % cleavages into S1/S2 and S2' are shown and were calculated as the ratio
1061 of the V5-immunoreactivity of the cleaved form to the sum of all forms. The data are representative
1062 of at least three independent experiments.

1063 Figure 3: **Processing of spike-glycoprotein at S2' is enhanced in presence of ACE2.** Western blot
1064 showing the impact of ACE2 on the processing of WT and μS1/S2 spike-glycoproteins by Furin.
1065 HeLa cells expressing empty vector (V), WT proS (**A**) or its μS1/S2 mutant (**B**) without or with
1066 Furin, ACE2 or both were analysed by Western blotting using anti-V5 antibody. The ratio of cDNAs
1067 used was S:ACE2:Furin = 1:1:1. The data are representative of at least three independent
1068 experiments.

1069 Figure 4: **Inhibition of PCs by BOS compounds.** (**A**) Chemical motif of BOS-inhibitors and
1070 representative structure of BOS-318. (**B**) *In vitro* BOS-inhibition of the cleavage of the fluorogenic
1071 dibasic substrate FAM-QRVRRAVGIDK-TAMRA by each of the proprotein convertases Furin,
1072 PC5 (PCSK5), PACE4 (PCSK6) and PC7 (PCSK7). All experiments were performed in 10
1073 different wells and the average pIC_{50} (in nM) was calculated. Shown for comparison is the
1074 inhibitory pIC_{50} of the Furin-like inhibitor RVKR-cmk performed >100 times. (**C**) *In vitro*
1075 inhibition of Furin by the BOS compounds. Furin (2 nM) was incubated with increasing
1076 concentration of BOS-inhibitors, and its enzymatic activity against the synthetic peptides
1077 DABSYL/Glu-TNSP<u>**RR**</u>A<u>**R**</u>↓SVAS-EDANS (5 μM) was measured at pH 7.5 (n=3). (**D**) Golgi
1078 assay: table representing the effects of BOS-inhibitors on U2OS cells expressing each of Furin,
1079 PC5A, PACE4 and PC7 simultaneously transduced with a BacMam-delivered construct

1080 containing a Golgi-targeting sequence followed by a 12-amino acid Furin/PCSK cleavage site
1081 from Bone Morphogenic Protein 10 (BMP10) and GFP at the C terminus (GalNAc-T2-GGGGS-
1082 DSTARIRR↓NAKG-GGGGS-GFP). Dibasic cleavage releases NAKG-GGGGS-GFP thereby
1083 reducing the Golgi-associated fluorescence estimated by imaging. (**E**) Furin-inhibitors (BOS)
1084 abrogate endogenous processing of the spike-glycoprotein. Hela cells were transiently transfected
1085 with a cDNA encoding an empty vector (V) or with one expressing the V5-tagged spike (S)
1086 glycoprotein (spike-V5). At 5h pre-transfection, cells were treated with vehicle DMSO (NT,
1087 duplicate) or with the Furin-inhibitors at indicated concentrations, or RVKR-cmk at 50 μM. At 24h
1088 post-transfection media were replaced with fresh ones lacking (NT) or containing the inhibitors for
1089 an additional 24h. Cell extracts were analyzed by Western blotting using a mAb-V5. All data are
1090 representative of at least three independent experiments.

1091 Figure 5: **Furin-like inhibitors and Camostat treatment decrease SARS-CoV-2 infection in**
1092 **Calu-3 Cells.** (**A**) Replication kinetics was studied at 12, 24 and 48h post-infection by plaque
1093 assay to determine PFUs of SARS-CoV-2 virus in the supernatant of infected Calu-3 cells treated
1094 or not with 1μM BOS-318, BOS-857 and BOS-981. A line graph represents results of the triplicate
1095 plaque assay results (mean ± SD). (**B**) The virus titers (PFU per milliliter) released in the
1096 supernatant (24h post-infection) of infected Calu-3 cells treated with indicated concentrations of
1097 BOS-318 were determined by plaque assay (mean ± SD of triplicates, *$p < 0.05$; **$p < 0.01$; ***p
1098 < 0.001) (left panel). The selectivity index (SI) of BOS-318 in Calu-3 cells as shown in top right
1099 panel was determined by CC_{50}/IC_{50}. The left y axis indicates the inhibition of virus titer (percent)
1100 relative to that of the untreated control group (red). The right y axis indicates the cell viability
1101 (percent) relative to that of the untreated control group (green). The CC_{50} (50% cytotoxic
1102 concentration), IC_{50} (half maximal inhibitory concentration), and SI (selectivity index) values for

1103 each inhibitor are as shown. Representative plaque images of infected Calu-3 cells treated with
1104 indicated doses of BOS-inhibitors are shown in the bottom right panel. (**C**) Immunoblots for the
1105 infected Calu-3 cells (right panel) and viral particles secreted in the supernatant (left panel) with
1106 and without treatment with BOS-inhibitors indicate reduced viral protein levels. Immunoblots
1107 were probed for the full-length (proSm) and cleaved (S2) fragments of viral S protein and
1108 nucleocapsid (N) protein as indicated; β-Actin was included as the loading control for the cells.
1109 (**D**) The virus titers (PFU per milliliter) released in the supernatant (24h post-infection) of infected
1110 Calu-3 cells treated with BOS-318 and/or Camostat (Camo) were determined by plaque assay
1111 (mean ± SD of duplicates, *, $p < 0.05$; **, $p < 0.01$; ***, $p < 0.001$) (top panel). Representative
1112 plaque images of infected Calu-3 cells are shown in the bottom panel. Color plaques differentiate
1113 the lawn (one color gray per well) from individual plaques (independent colors).

1114 Figure 6: **Processing of SARS-CoV-2 S by Furin-like convertases and TMPRSS2 is critical**
1115 **for viral entry in human lung epithelial cells but not in model HEK293 cells stably expressing**
1116 **ACE2**. (**A**) Furin cleavage of proS at the S1/S2 site is required for SARS-CoV-2 pseudoviral entry
1117 in Calu-3 cells but not HEK293T-ACE2 cells. Cells were inoculated with nanoluciferase-
1118 expressing HIV particles pseudotyped with SARS-CoV-2: wild-type spike (WT), double Ala-
1119 mutant spike (μS1/S2) or Furin-optimized spike (μS2'). Inhibition of proS processing at S1/S2 by
1120 a novel Furin-like inhibitor (BOS-318) during pseudovirion packaging prevents viral entry in
1121 Calu-3 cells but not in HEK293T-ACE2 cells. (**B**) Western blot analyses show inhibition by BOS-
1122 318 of proS processing at S1/S2 site. Purified pseudovirions and cellular extracts of producing
1123 HEK293-T17 cells treated or not with BOS-318 inhibitor were separated on SDS-PAGE gel and
1124 analyzed for HIV-1 p24 and V5-tagged S-protein (proSm or cleaved, S2) as indicated. (**C**) Pre-
1125 treatment of Calu-3 cells with (B) 1 μM BOS-318, (C) 100 μM Camostat or both (B+C) markedly

1126 reduces viral entry. In Panels A and C, Calu-3 cells were transduced with nanoluciferase-
1127 expressing HIV particles pseudotyped with SARS-CoV-2 S WT, μS1/S2 or μS2' for 72h and
1128 analyzed for nano-luciferase expression. Viral entry was expressed as fold increase over that given
1129 by bald particles (pseudovirions made in the absence of S). In panels **A** and **C** each dot represents
1130 a different experiment with median luciferase activity calculated from three biological replicates.
1131 Two to four experiments were performed for each cell type. Error bars indicate standard deviation
1132 (SD) from the mean.

1133 Figure 7: **Spike-induced cell-to-cell fusion relies on Furin cleavage at S1/S2.** (**A**) Cell-to-cell
1134 fusion between donor cells (HeLa) expressing the fusogenic SARS-CoV-2 spike protein along
1135 with the HIV trans-activator Tat, and acceptor cells (TZM-bl) that express ACE2. Upon fusion,
1136 Tat is transferred from donor to acceptor cells, thereby inducing luciferase expression. (**B**) Cell-
1137 to-cell fusion was evaluated using confocal microscopy. A representative immunocytochemistry
1138 of Hela cells transfected with a vector expressing SARS-CoV-2 spike co-cultured with TZM-bl
1139 cells for 18h. The number of syncytia (multiple nuclei) was examined using CellMask™ to probe
1140 for the plasma membrane and Dapi to stain the nuclei. (**C**) Donor cells were transfected with
1141 vectors expressing either no protein (empty vector, V), μS1/S2, or WT-spike (S) in the absence
1142 (NT) or presence of vehicle (DMSO) or with the Furin-inhibitors BOS-318, BOS-981, BOS-857
1143 (300 nM) or RVKR (10 μM). Acceptor cells were transfected with a vector expressing ACE2.
1144 After 48h, donor and acceptor cells were co-cultured for 18h. Relative luminescence units (RLU)
1145 were normalized to the V value arbitrarily set to 1. Data are presented as mean values ± SD (n=3),
1146 One-Way ANOVA, Dunn-Sidàk multiple comparison test. (**D**) Donor HeLa cells expressing WT-
1147 S or its indicated mutants and variants were co-cultured with acceptor TZM-bl cells expressing
1148 ACE2. The extent of fusion is represented as a ratio between the RLU measured for each condition

1149 and that of donor cells expressing empty vector. The bar graph represents the average of 3
1150 experiments performed in triplicates. Data are presented as mean values ± SEM (n=3), One-way
1151 Anova Bonferroni multiple comparison test. Two-Way ANOVA, Dunn-Sidàk multiple
1152 comparison test.

1153 Figure 8: **Spike-glycoprotein processing by Furin and TMPRSS2 in a co-culture system and**
1154 **their role in cell-to-cell fusion.** Donor HeLa cells expressing empty vector (V), WT-S-HA or
1155 μS1/S2-HA were co-cultured with acceptor TZM-bl cells expressing V, ACE2, or ACE2 +
1156 TMPRSS2 (TMP). From the same experiment, cell-to-cell fusion (**A**) was assessed in parallel by
1157 Western blotting of spike-glycoproteins in cells and media using an anti-V5 mAb (**B**). Secreted
1158 forms of spike protein (S1) in the media were detected with anti HA-HRP upon
1159 immunoprecipitation with anti-HA agarose. The bar graph shows one representative fusion assay
1160 done un duplicate. The corresponding Western-blot is representative of three independent
1161 experiments. Values of S2 and S2' relative to β-actin are shown (nd = too low or not detected).

1162 Figure 9: **Exogenous TMPRSS2-generated shedding of ACE2 differentially regulates S-induced**
1163 **fusion at the plasma membrane of WT-S *versus* μAS1/S2.** Donor HeLa cells expressing double
1164 tagged (N-terminal HA-tag; C-terminal V5-tag) spike-glycoprotein WT (S) or its S1/S2 mutant
1165 (μAS1/S2) were co-cultured with acceptor TZM-bl cells expressing (empty vector, V), ACE2, or
1166 ACE2 + TMPRSS2 (TMP) and treated with DMSO (vehicle control) or Camostat (120 μM).
1167 Within the same experiment, cell-to-cell fusion (**A**) was assessed in parallel with spike processing
1168 in cells and media by Western-blot (**B, C**). (**A**) The extent of fusion is represented as a ratio
1169 between the RLU measured for each condition and that of donor cells expressing V. The bar graph
1170 represents the average of 2 experiments performed in triplicates. (**B, C**). Western blot analyses of
1171 media and cell extracts of the co-cultured cells with donor cells overexpressing double tagged (N-

1172 terminal HA-tag; C-terminal V5-tag) spike-glycoprotein, WT (S) (**B**) or μAS1/S2 (**C**). The arrow
1173 points to a putative degradation product of S2', that is absent in presence of Camostat. Media were
1174 subjected to immunoprecipitation with anti-HA agarose for the secreted forms of spike protein (S1,
1175 $S1_L$) followed by Western blotting with anti HA-HRP. In the cell extracts Spike-glycoproteins and
1176 ACE2 were immunoblotted with anti-V5 mAb and a polyclonal ACE2 antibody, respectively. The
1177 data are representative of three independent experiments.

1178 Figure 10: **The C-terminal collectrin-like domain of ACE2 may be critical for the regulation**
1179 **of cell-to-cell fusion of spike-glycoprotein when exogenous TMPRSS2 is present.** (**A**)
1180 Schematic representation of the primary structure of human ACE2 with emphasis on the C-
1181 terminal collectrin-like domain (aa 616-768, light gray), TMPRSS2 cleavage region (aa 697-716,
1182 black) and the polybasic amino-acid segments in which K/R were mutated to A (C0 and C4)
1183 (amino acids underlined and in bold). Also shown are the peptidase domain (aa 19-615, white)
1184 containing the regions involved in the interaction with the spike SARS-CoV protein (hatched) and
1185 transmembrane domain (TM). (**B**) HeLa cells were co-transfected with ACE2, WT (ACE2) or its
1186 mutant ACE2 (C0+C4), and TMPRSS2, WT (TMPRSS2) or its S441A active-site mutant
1187 (μTMPRSS2), or empty vector (V). Media and cell extracts were analyzed by western blotting for
1188 shed ACE2 (sACE2) and ACE2, respectively. The migration positions of the ~95 kDa and ~80
1189 kDa sACE2 are emphasized. (**C**) Donor HeLa cells expressing WT-S-HA or μAS1/S2-HA were
1190 co-cultured with acceptor TZM-bl cells expressing ACE2, WT (ACE2) or its mutant ACE2
1191 (C0+C4) in presence or absence of TMPRSS2. From the same experiment, cell-to-cell fusion was
1192 assessed (**C**), in parallel with WB analyses of cells and media (**D**). The extent of fusion is
1193 represented as a ratio between the RLU measured for each condition and that of donor cells
1194 expressing an empty vector. The bar graph represents the average of 3 experiments performed in
1195 triplicates. Data are presented as mean values ± SD (n=3), One-way Anova Turkey's multiple

1196 comparison test. (**D**) Co-culture media were subjected to immunoprecipitation with anti-HA
1197 agarose for the secreted forms of spike protein (S1) followed by western blot with anti HA-HRP.
1198 Spike-glycoproteins in the cell extracts were immunoblotted with anti-V5 mAb. The Western blot
1199 data are representative of three independent experiments.

1200 Figure 11: **Proposed model for the processing of S-protein and its blockade by Furin and**
1201 **TMPRSS2 inhibitors.** Boxed left panel: schematic representation of the S-glycoprotein domains
1202 of SARS-CoV-2, including the N-terminal (NTD) and C-terminal (CTD) domains of S1, the Furin-
1203 S1/S2 and the Furin/TMPRSS2-S2' processing sites as well as the fusogenic α-helix that follows
1204 S2'. Binding of the RBD domain of S1 to the membrane associated ACE2 in target cells, and the
1205 cell surface expression of TMPRSS2 and Furin are also schematized. Right panels: (**1**) BOS-
1206 inhibitors (or μS1/S2 mutant) completely prevent cell-to-cell fusion of donor Hela cells expressing
1207 S-glycoprotein with acceptor HeLa-ACE2 cells, which lack endogenous TMPRSS2. In this
1208 context, this reveals that Furin is a major processing enzyme cleaving at S1/S2 and generating S2'.
1209 (**2**) In acceptor HeLa cells expressing TMPRSS2 (+), maximal prevention of cell-to-cell fusion
1210 can be achieved by a combination of Furin (BOS, phenocopying the μS1/S2 or μAS1/S2 mutants)
1211 and TMPRSS2 (Camostat) inhibitors blocks S2' production, ACE2-shedding (sACE2) and the
1212 separation of sACE2-$S1_L$ complex from S2. (**3**) Optimal blockade of SARS-CoV-2 infection of
1213 Calu-3 cells, which express endogenously both Furin and TMPRSS2, is also achieved by a
1214 combination of Furin (BOS) and TMPRSS2 (Camostat) inhibitors.

1215

1216 **SUPPORTING INFORMATION (SI): TABLE 1; FIGURES 1-7**

1217 Table 1: **Sequences of the different peptides mimicking the Cov spike cleavage sites that have**
1218 **been tested in the enzymatic assay.** The arrow indicates the expected cleavage site.

1219 SI-Figure 1: **Importance of Furin in the processing of the Spike-glycoprotein.** (**A**) HeLa cells
1220 were first transfected with control non-targeting siRNA (siCTL) or siRNA Furin (siFur) at final
1221 concentrations of 20 nM, or mock transfected (N) and 24h later, transfected with empty vector (V)
1222 or with that coding for a V5-tagged spike-glycoprotein for an additional 48h. Following lysis,
1223 proteins were resolved on SDS-PAGE followed by WB with anti-V5 or anti-Furin antibodies. (**B**)
1224 HeLa cells transfected with empty vector (V), V5-tagged wild type spike-protein (WT) or its S1/S2
1225 site mutant (µS1/S2) were treated with Endo-F and Endo-H or mock treated (NT) and analyzed as
1226 described in panel A. (**C, D**) HeLa cells transfected with V5-tagged wild type spike-protein (WT)
1227 or S1/S2 single mutants (**C**) or S2' single or double mutants (**D**) in the absence (V) or presence of
1228 overexpressed Furin were lysed and analyzed by WB.

1229 SI-Figure 2: **Immunocytochemistry of the co-localization of ACE2 and S-protein or µS1/S2-**
1230 **S in HeLa cells.** Immunofluorescence of S-protein (green), WT (S) or µS1/S2, and ACE2 (red)
1231 were revealed using the spike S2-antibody GTX632604 in non-permeabilized (NP) conditions or
1232 anti-V5 in permeabilized (P) conditions, and ACE2 antibody AF933. The confocal co-localizations
1233 are shown in the merged Figures. Scale bar = 10 µm.

1234 SI-Figure 3: **Furin-like inhibitors strongly reduce SARS-CoV-2 infection in Calu-3 cells.**
1235 Calu-3 cells were treated with indicated concentrations of (**A**) BOS-857 and (**B**) BOS-981 and
1236 infected with SARS-CoV-2 for 24h. Virus titers in the supernatant were determined by plaque
1237 assay on VeroE6 cells (mean plaque forming units [PFU] per ml) ± SD of triplicates, $^{*}p <$
1238 0.05; $^{**}p < 0.01$; $^{***}p < 0.001$). The selectivity index (SI) of (**A**) BOS-857, and (**B**) BOS-981 in

1239 Calu-3 cells as shown in top right panel was determined by CC_{50}/IC_{50}. The left y axis indicates
1240 the inhibition of virus titer (percent) relative to that of the untreated control group (red). The
1241 right y axis indicates the cell viability (percent) relative to that of the untreated control group
1242 (green). Representative plaque images of infected Calu-3 cells treated with indicated doses of
1243 BOS-inhibitors are shown in the bottom right panel. Color plaques differentiate the lawn (one
1244 color gray per well) from individual plaques (independent colors).

1245 SI-Figure 4: **Furin-like inhibitors modestly reduce virus production in SARS-CoV-2-infected**
1246 **Vero E6 cells in a concentration-dependent manner. (A)** Vero E6 cells treated or not with 1μM
1247 BOS-318, BOS-857 or BOS-981 were infected with SARS-CoV-2 for up to 45h. Virus titers in
1248 the supernatant obtained at 12, 24 and 48 h post infection were determined by plaque assay on
1249 Vero E6. A line graph represents results of the triplicate plaque assay (mean PFU/ml ± SD). **(B,**
1250 **C, and D)** Virus released in the supernatant (48 hr post infection) of infected Vero E6 cells treated
1251 with indicated concentrations of (B) BOS-318, (C) BOS-857, or (D) BOS-981 were determined
1252 by plaque assay (mean ± SD of triplicates, $*p < 0.05$; $**p < 0.01$; $***p < 0.001$).

1253 SI-Figure 5: **Combination of BOS-981 and Camostat reduces SARS-CoV-2 replication.** Calu-
1254 3 cells were treated with BOS-981 and/or Camostat (Camo) and infected with SARS-CoV-2 for
1255 24h. Virus titers in the supernatant were determined by plaque assay on VeroE6 (mean PFU/ml ±
1256 SD of duplicates, $^{*}p< 0.05$. Representative plaque images of infected Calu-3 cells are shown in the
1257 bottom panel. Color plaques differentiate the lawn (one color gray per well) from individual
1258 plaques (independent colors).

1259 SI-Figure 6: **Cell-to-cell fusion assay: correlation between syncytia formation and luciferase**
1260 **activity.** (**A**) Cell-to-cell fusion between donor cells (HeLa) and acceptor cells (TZM-bl) was
1261 evaluated using confocal microscopy. Hela cells transfected with: (**a**) an empty vector (V), or

1262 expressing (**b**) HIV-gp160 and Tat, (**c**) SARS-CoV-2 spike, or (**d**) μS1/S2 were co-cultured with
1263 TZM-bl cells for 18h and the number of syncytia was examined using CellMask™ to probe for
1264 the plasma membrane and Dapi to stain the nuclei. (**B)** Donor cells were transfected with vectors
1265 expressing either no protein (V), Tat, WT-spike (S), Tat and WT-spike (Tat + S) or Tat and HIV-
1266 gp160 (Tat + gp160). Acceptor cells were transfected with a vector expressing no protein (V), with
1267 ACE2 or directly with Tat as a positive control (hatched bar). After 48h, cells were co-cultured for
1268 18h. Luminescence was normalized to the V value arbitrarily set to 1. Data are presented as mean
1269 values ± SD (n=3) and a representative experiment is shown. (**C)** Donor cells were transfected
1270 with increasing amount of plasmid expressing WT-spike and acceptor cells were transfected with
1271 a vector expressing ACE2. After 48h, cells were co-cultured for 18h, and prepared for
1272 luminescence or microscopy. Correlation between the number of syncytia counted by microscopy
1273 (n=10 per condition) and the luciferase activity was determined, and the calculated correlation
1274 coefficient is R^2=0.87.

1275 SI-Figure 7: **Secretion of S1.** HeLa cells were transiently co-expressed with double-tagged spike
1276 protein (N-terminal HA-tag; C-terminal V5-tag), WT (S) or its mutants, μS1/S2 or μAS1/S2, and
1277 ACE2 alone or in combination with TMPRSS2, WT (TMPRSS2) or its S441A active-mutant
1278 (μTMPRSS2), at a ratio S:ACE2:TMPRSS2 = 1:0.5:0.5. Immunoblot of the 24h conditioned
1279 media was first probed for secreted S1, S1' and $S1_L$ (HA-HRP antibody), stripped and next probed
1280 for shed ACE2 (sACE2).

Figure 1

A

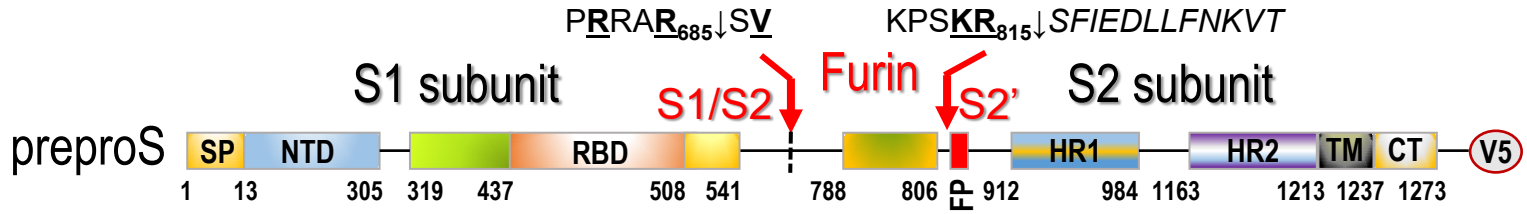
PRRAR685↓SV
KPSKR815↓SFIEDLLFNKVT
S1 subunit
S1/S2
Furin
S2'
S2 subunit
preproS
SP
NTD
RBD
HR1
HR2
TM
CT
V5
FP
1
13
305
319
437
508
541
788
806
912
984
1163
1213
1237
1273

B

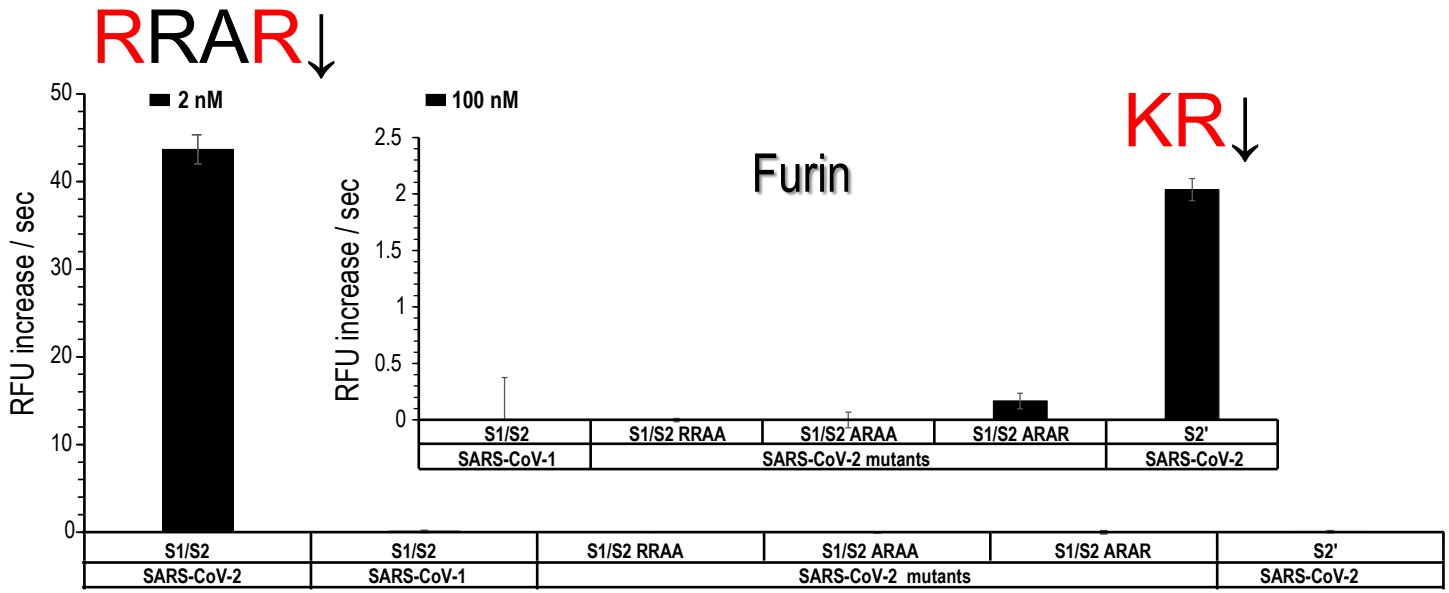
RRAR↓
2 nM
100 nM
Furin
KR↓
RFU increase / sec
S1/S2
SARS-CoV-2
S1/S2
SARS-CoV-1
S1/S2 RRAA
S1/S2 ARAA
S1/S2 ARAR
SARS-CoV-2 mutants
S2'
SARS-CoV-2

C

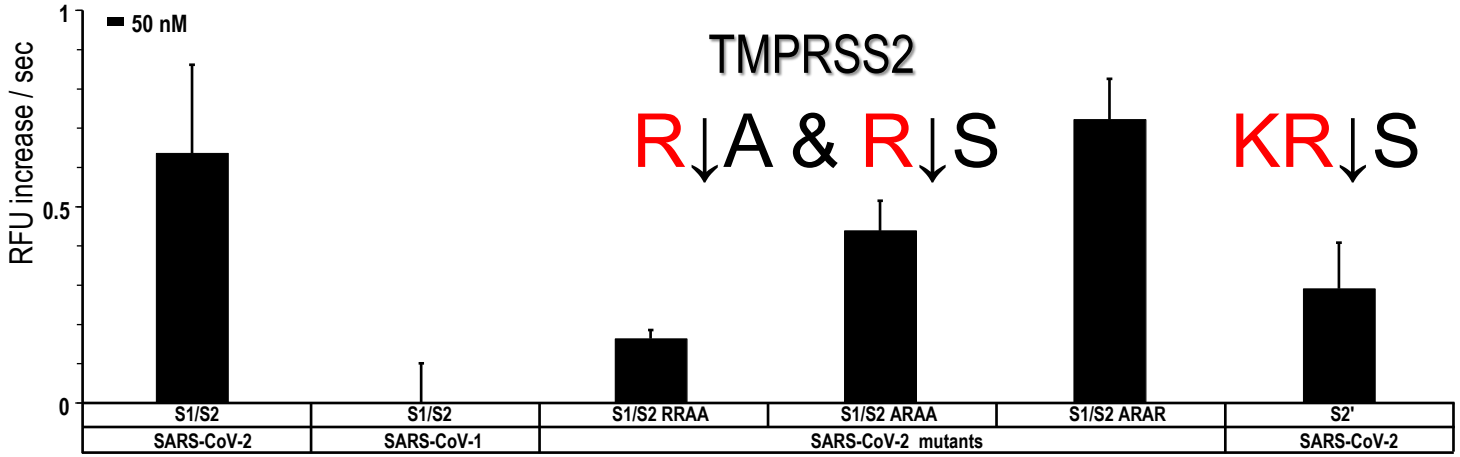
50 nM
TMPRSS2
R↓A & R↓S
KR↓S
RFU increase / sec
S1/S2
SARS-CoV-2
S1/S2
SARS-CoV-1
S1/S2 RRAA
S1/S2 ARAA
S1/S2 ARAR
SARS-CoV-2 mutants
S2'
SARS-CoV-2

Figure 1: **Processing of S-peptides by Furin and TMPRSS2.** (**A**) Schematic representation of the primary structure of preproS and its domains and the predicted Furin-like S1/S2 site generating the S1- and S2-subunits, as well as the S2' site preceding the fusion peptide (FP). The signal peptide (SP), N-terminal domain (NTD), receptor binding domain (RBD) to ACE2, the two heptad repeats HR1 and HR2, the transmembrane domain (TM), the cytosolic tail (CT) and the C-terminal V5-tag are indicated. (**B**) *In vitro* Furin activity against peptides mimicking the S1/S2 (and its mutants) and S2' cleavage site sequence of the spike protein from SARS-CoV-2 and SARS-CoV-1, as described in SI-Table 1. Each substrate was tested at a final protease concentration of 2 and 100 nM. (**C**) *In vitro* TMPRSS2 activity (at 50 nM) against peptides mimicking the S1/S2 and S2' cleavage site sequence of the spike protein from SARS-CoV-2 (and its mutants) described in SI-Table 1.

Figure 2

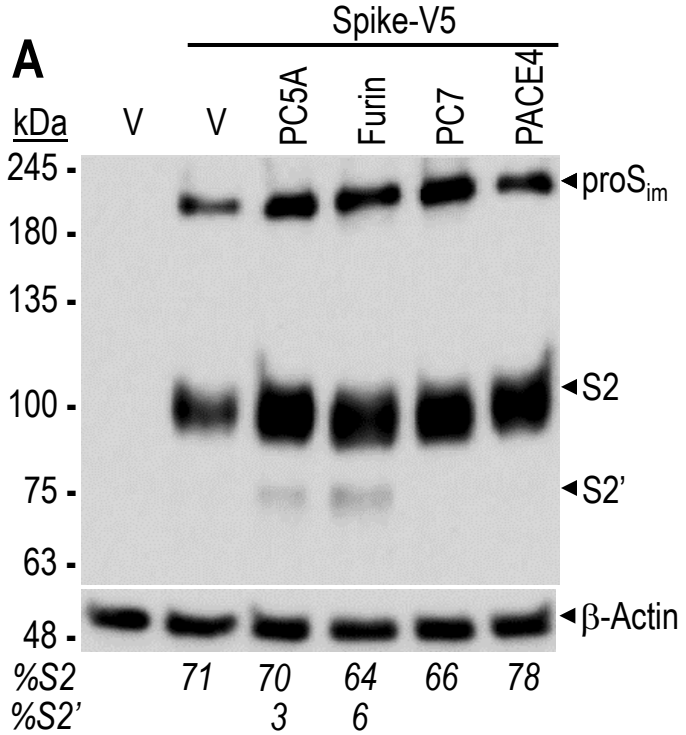
A
Spike-V5
kDa
V
V
PC5A
Furin
PC7
PACE4
245
180
135
100
75
63
48
proS$_{im}$
S2
S2'
β-Actin
%S2
71
70
64
66
78
%S2'
3
6

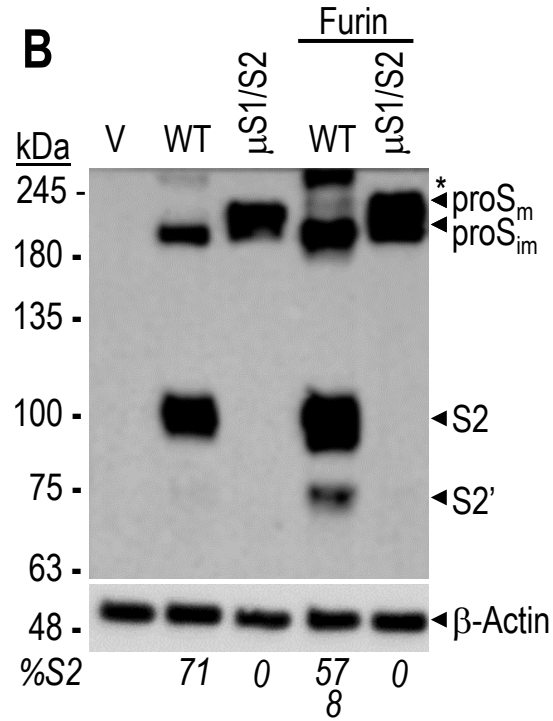
B
Furin
kDa
V
WT
μS1/S2
WT
μS1/S2
245
180
135
100
75
63
48
*
proS$_m$
proS$_{im}$
S2
S2'
β-Actin
%S2
71
0
57
0
8

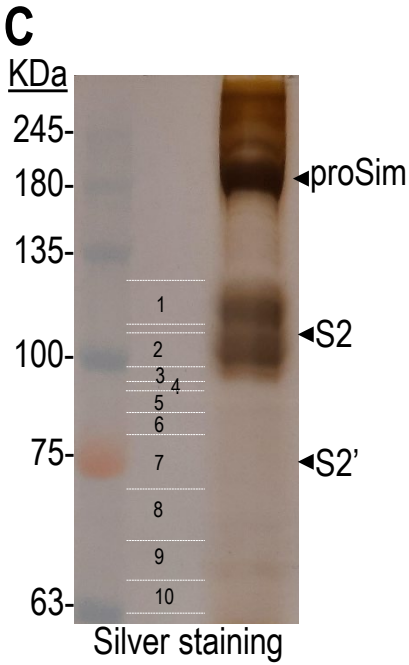
C
KDa
245
180
135
100
75
63
proSim
S2
S2'
1
2
3
4
5
6
7
8
9
10
Silver staining

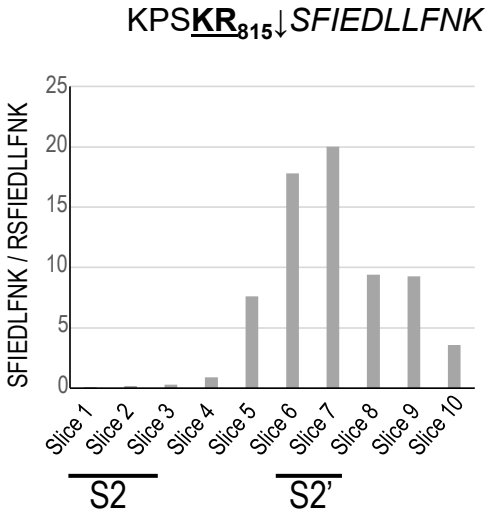
KPSKR$_{815}$↓SFIEDLLFNK
SFIEDLFNK / RSFIEDLLFNK
25
20
15
10
5
0
Slice 1
Slice 2
Slice 3
Slice 4
Slice 5
Slice 6
Slice 7
Slice 8
Slice 9
Slice 10
S2
S2'

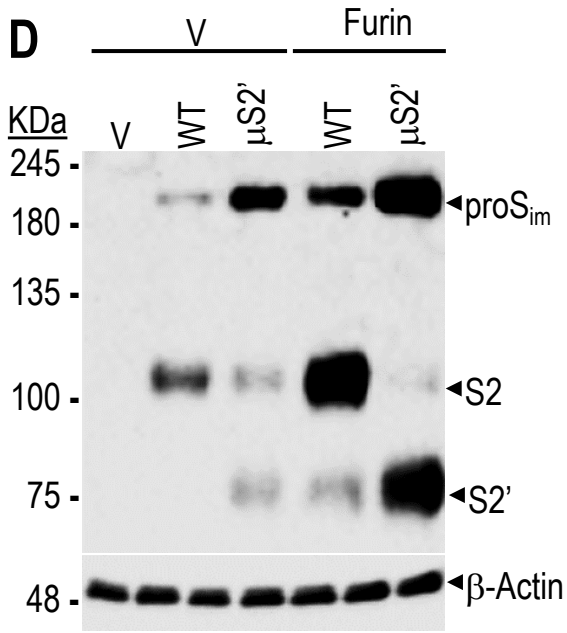
D
V
Furin
KDa
V
WT
μS2'
WT
μS2'
245
180
135
100
75
48
proS$_{im}$
S2
S2'
β-Actin

Figure 2: **Processing of spike-glycoprotein in HeLa cells.** (**A**) Western blot analyses of the processing of WT proS into V5-tagged S2 and S2' by the proprotein convertases Furin, PC5A, PACE4 and PC7 following co-transfection of their cDNAs in HeLa cells. The migration positions of immature proSim, S2 and S2' as well as the β-Actin loading control are emphasized. V = empty pIRES-EGFP-V5 vector. (**B**) Western blot analyses of HeLa cells following co-transfection with cDNAs coding for either WT-S-protein or its double Ala-mutant [R685A + R682A] (μS1/S2) in the absence or presence of Furin cDNA at a ratio S:protease = 1:2. *Inconsistently observed oligomeric forms of proS. (**C**) Identification of S2' cleavage site by MS/MS. WT-spike-glycoprotein was immunoprecipitated from HeLa cells using V5 agarose beads then resolved by SDS electrophoresis SDS/PAGE and subjected to silver staining (left panel); the positions of the slices are indicated (1 to 10). The MS/MS analysis of peptides generated by a Lys-specific protease (K814↓) are indicated; the data represent the ratio of SFIEDLLFNK$_{825}$ to R$_{815}$SFIEDLLFNK$_{825}$ (right panel). (**D**) Western blot analyses of HeLa cells co-transfected with V5-tagged spike protein, WT (S) or its Furin-optimized S2' (KRRKR$_{815}$↓SF) mutant (μS2'), and empty vector (V) or Furin. (**A**, **B**) The estimated % cleavages into S1/S2 and S2' are shown and were calculated as the ratio of the V5-immunoreactivity of the cleaved form to the sum of all forms. The data are representative of at least three independent experiments.

Figure 3

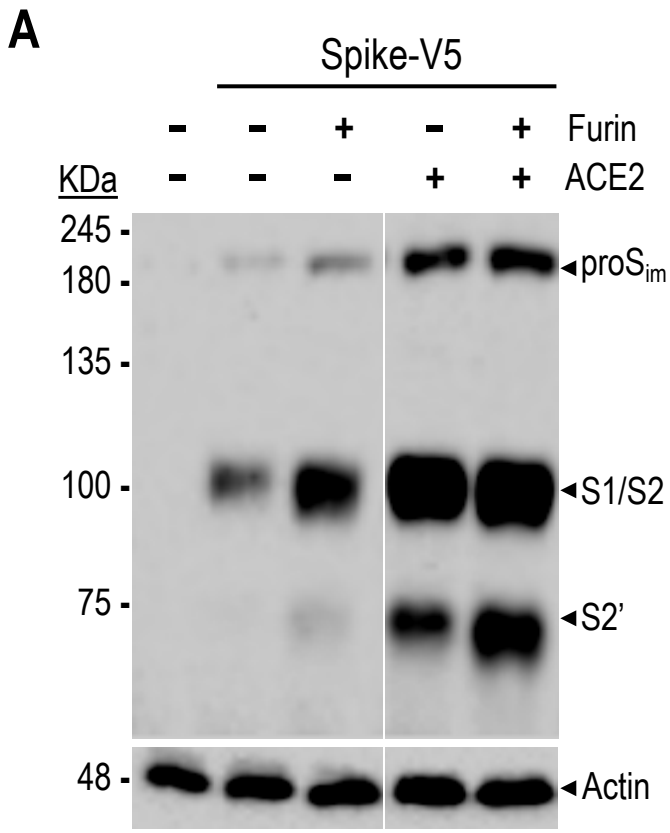
A
Spike-V5
Furin
ACE2
KDa
245
180
135
100
75
48
proS$_{im}$
S1/S2
S2'
Actin

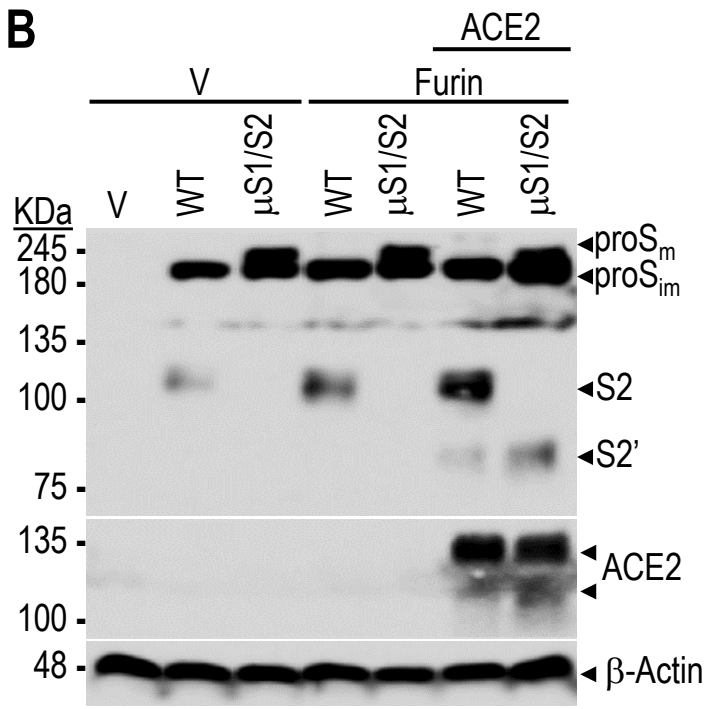
B
ACE2
V
Furin
KDa
V
WT
μS1/S2
WT
μS1/S2
WT
μS1/S2
245
180
135
100
75
135
100
48
proS$_m$
proS$_{im}$
S2
S2'
ACE2
β-Actin

Figure 3: **Processing of spike-glycoprotein at S2' is enhanced in presence of ACE2.** Western blot showing the impact of ACE2 on the processing of WT and μS1/S2 spike-glycoproteins by Furin. HeLa cells expressing empty vector (V), WT proS (**A**) or its μS1/S2 mutant (**B**) without or with Furin, ACE2 or both were analysed by Western blotting using anti-V5 antibody. The ratio of cDNAs used was S:ACE2:Furin = 1:1:1. The data are representative of at least three independent experiments.

Figure 4

A

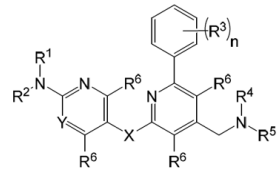

Structure of Furin inhibitors

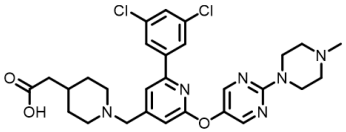

BOS-318

B

	Furin pIC50	PC5 pIC50	PACE4 pIC50	PC7 pIC50
BOS-318	8.8±0.4 (n=10)	6.7±0.15 (n=8)	6.7±0.15 (n=6)	7.4±0.22 (n=8)
BOS-981	9.3±0.5 (n=10)	7.5±0.22 (n=10)	6.9±0.1 (n=4)	6.9±0.2 (n=8)
BOS-857	9.4±0.3 (n=10)	7.6±0.2 (n=10)	6.7±0.24 (n=5)	6.9±0.3 (n=8)
decanoyl-RVKR-cmk	9.1±0.43 (n=447)	9.9±0.38 (n=162)	9.2±0.24 (n=214)	9.6±0.63 (n=198)

C

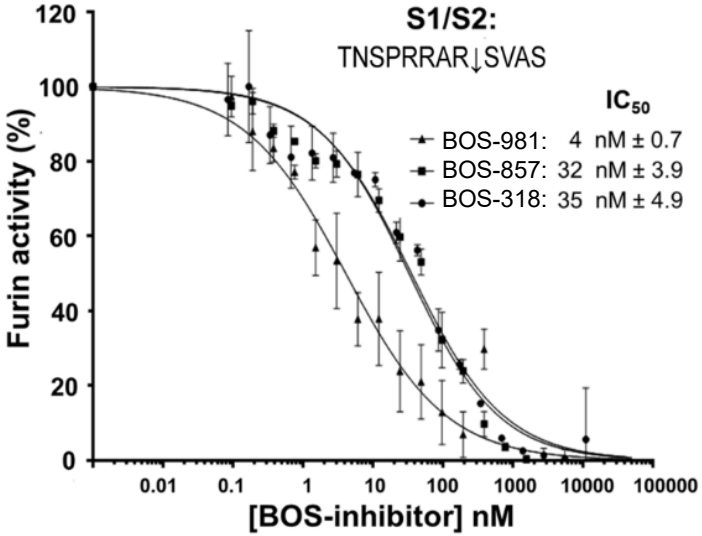

D

	Golgi pIC50 (U20S)
BOS-318	7.7±0.24 (n=22)
BOS-981	8.3±0.25 (n=12)
BOS-857	7.6±0.2 (n=12)
decanoyl-RVKR-cmk	5.1±0.33 (n=8)

E

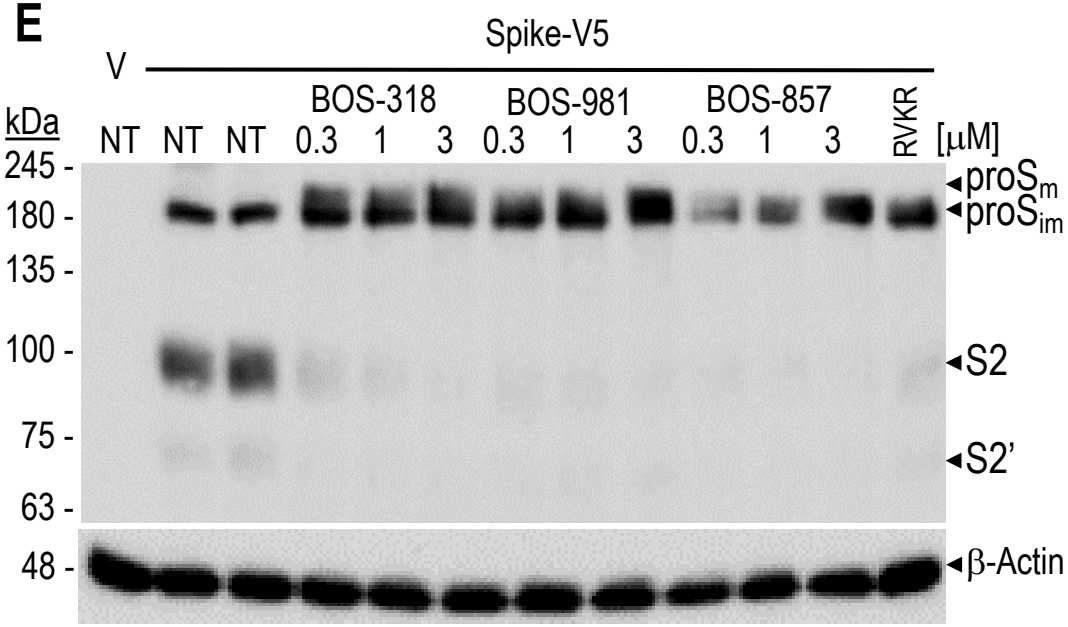

HeLa-ACE2

Figure 4: **Inhibition of PCs by BOS compounds.** (**A**) Chemical motif of BOS-inhibitors and representative structure of BOS-318. (**B**) *In vitro* BOS-inhibition of the cleavage of the fluorogenic dibasic substrate FAM-QRVRRAVGIDK-TAMRA by each of the proprotein convertases Furin, PC5 (PCSK5), PACE4 (PCSK6) and PC7 (PCSK7). All experiments were performed in 10 different wells and the average pIC_{50} (in nM) was calculated. Shown for comparison is the inhibitory pIC_{50} of the Furin-like inhibitor dec-RVKR-cmk performed >100 times. (**C**) *In vitro* inhibition of Furin by the BOS compounds. Furin (2 nM) was incubated with increasing concentration of BOS-inhibitors, and its enzymatic activity against the synthetic peptides DABSYL/Glu-TNSP**RR**A**R**↓SVAS-EDANS (5 μM) was measured at pH 7.5 (n=3). (**D**) Golgi assay: table representing the effects of BOS-inhibitors on U2OS cells expressing each of Furin, PC5A, PACE4 and PC7 simultaneously transduced with a BacMam-delivered construct containing a Golgi-targeting sequence followed by a 12-amino acid Furin/PCSK cleavage site from Bone Morphogenic Protein 10 (BMP10) and GFP at the C terminus (GalNAc-T2-GGGGS-DSTARIRR↓NAKG-GGGGS-GFP). Dibasic cleavage releases NAKG-GGGGS-GFP thereby reducing the Golgi-associated fluorescence estimated by imaging. (**E**) Furin-inhibitors (BOS) abrogate endogenous processing of the spike-glycoprotein. Hela cells were transiently transfected with a cDNA encoding an empty vector (V) or with one expressing the V5-tagged spike (S) glycoprotein (spike-V5). At 5h pre-transfection, cells were treated with vehicle DMSO (NT, duplicate) or with the Furin-inhibitors at indicated concentrations, or RVKR-cmk at 50 μM. At 24h post-transfection media were replaced with fresh ones lacking (NT) or containing the inhibitors for an additional 24h. Cell extracts were analyzed by Western blotting using a mAb-V5. All data are representative of at least three independent experiments.

Figure 5

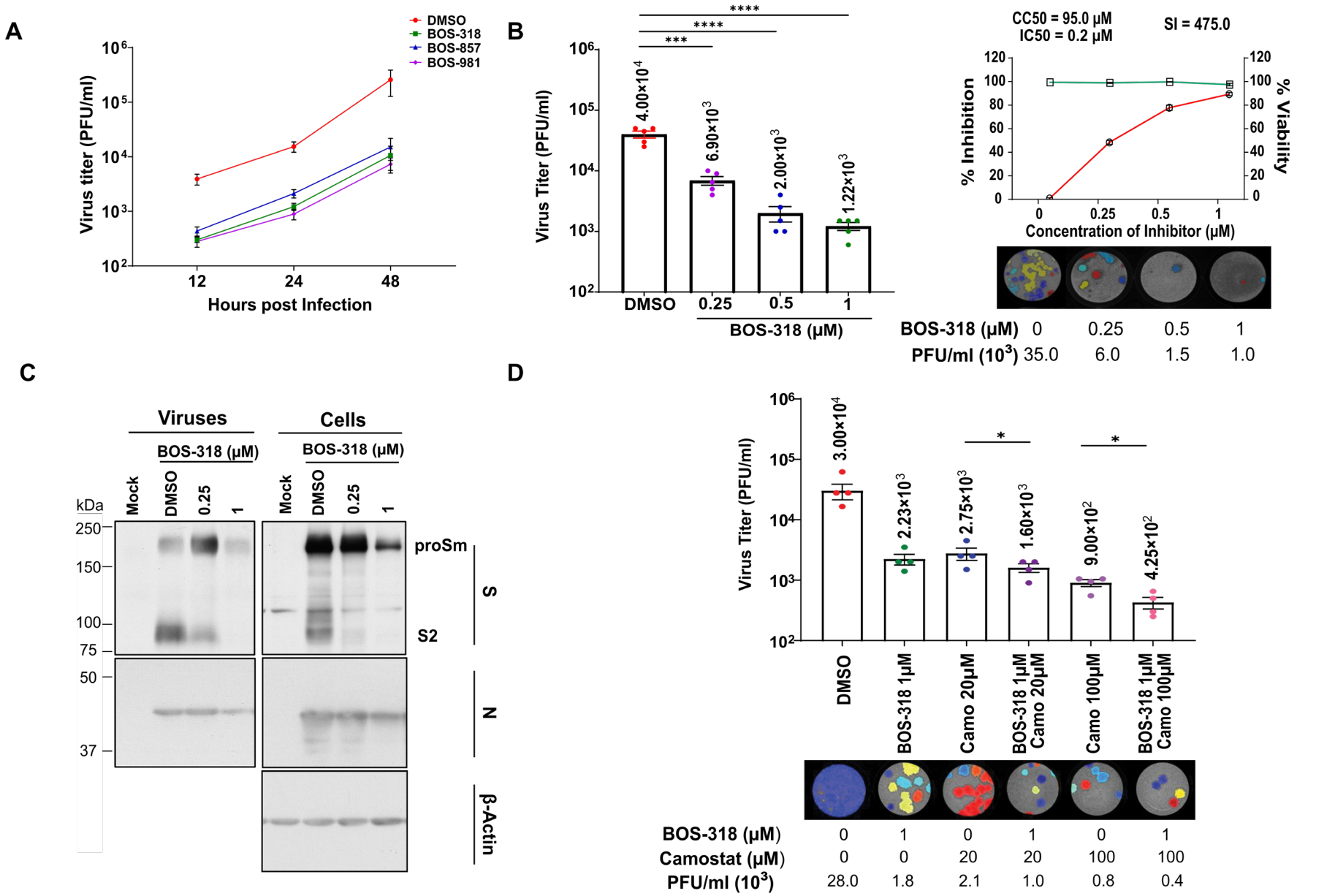
A
DMSO
BOS-318
BOS-857
BOS-981
Virus titer (PFU/ml)
Hours post Infection
B
Virus Titer (PFU/ml)
4.00×10^4
6.90×10^3
2.00×10^3
1.22×10^3
DMSO
0.25
0.5
1
BOS-318 (μM)
CC50 = 95.0 μM
IC50 = 0.2 μM
SI = 475.0
% Inhibition
% Viability
Concentration of Inhibitor (μM)
BOS-318 (μM) 0 0.25 0.5 1
PFU/ml (10^3) 35.0 6.0 1.5 1.0
C
Viruses
Cells
BOS-318 (μM)
Mock
DMSO
0.25
1
kDa
proSm
S2
S
N
β-Actin
D
Virus Titer (PFU/ml)
3.00×10^4
2.23×10^3
2.75×10^3
1.60×10^3
9.00×10^2
4.25×10^2
DMSO
BOS-318 1μM
Camo 20μM
BOS-318 1μM Camo 20μM
Camo 100μM
BOS-318 1μM Camo 100μM
BOS-318 (μM) 0 1 0 1 0 1
Camostat (μM) 0 0 20 20 100 100
PFU/ml (10^3) 28.0 1.8 2.1 1.0 0.8 0.4

Figure 5: **Furin-like inhibitors and Camostat treatment decrease SARS-CoV-2 infection in Calu-3 Cells.** (**A**) Replication kinetics was studied at 12, 24 and 48h post-infection by plaque assay to determine PFUs of SARS-CoV-2 virus in the supernatant of infected Calu-3 cells treated or not with 1μM BOS-318, BOS-857 and BOS-981. A line graph represents results of the triplicate plaque assay results (mean ± SD). (**B**) The virus titers (PFU per milliliter) released in the supernatant (24h post-infection) of infected Calu-3 cells treated with indicated concentrations of BOS-318 were determined by plaque assay (mean ± SD of triplicates, *$p < 0.05$; **$p < 0.01$; ***$p < 0.001$) (left panel). The selectivity index (SI) of BOS-318 in Calu-3 cells as shown in top right panel was determined by CC_{50}/IC_{50}. The left y axis indicates the inhibition of virus titer (percent) relative to that of the untreated control group (red). The right y axis indicates the cell viability (percent) relative to that of the untreated control group (green). The CC_{50} (50% cytotoxic concentration), IC_{50} (half maximal inhibitory concentration), and SI (selectivity index) values for each inhibitor are as shown. Representative plaque images of infected Calu-3 cells treated with indicated doses of BOS-inhibitors are shown in the bottom right panel. (**C**) Immunoblots for the infected Calu-3 cells (right panel) and viral particles secreted in the supernatant (left panel) with and without treatment with BOS-inhibitors indicate reduced viral protein levels. Immunoblots were probed for the full-length (proSm) and cleaved (S2) fragments of viral S protein and nucleocapsid (N) protein as indicated; β-Actin was included as the loading control for the cells. (**D**) The virus titers (PFU per milliliter) released in the supernatant (24h post-infection) of infected Calu-3 cells treated with BOS-318 and/or Camostat (Camo) were determined by plaque assay (mean ± SD of duplicates, *, $p < 0.05$; **, $p < 0.01$; ***, $p < 0.001$) (top panel). Representative plaque images of infected Calu-3 cells are shown in the bottom panel. Color plaques differentiate the lawn (one color gray per well) from individual plaques (independent colors).

Figure 6

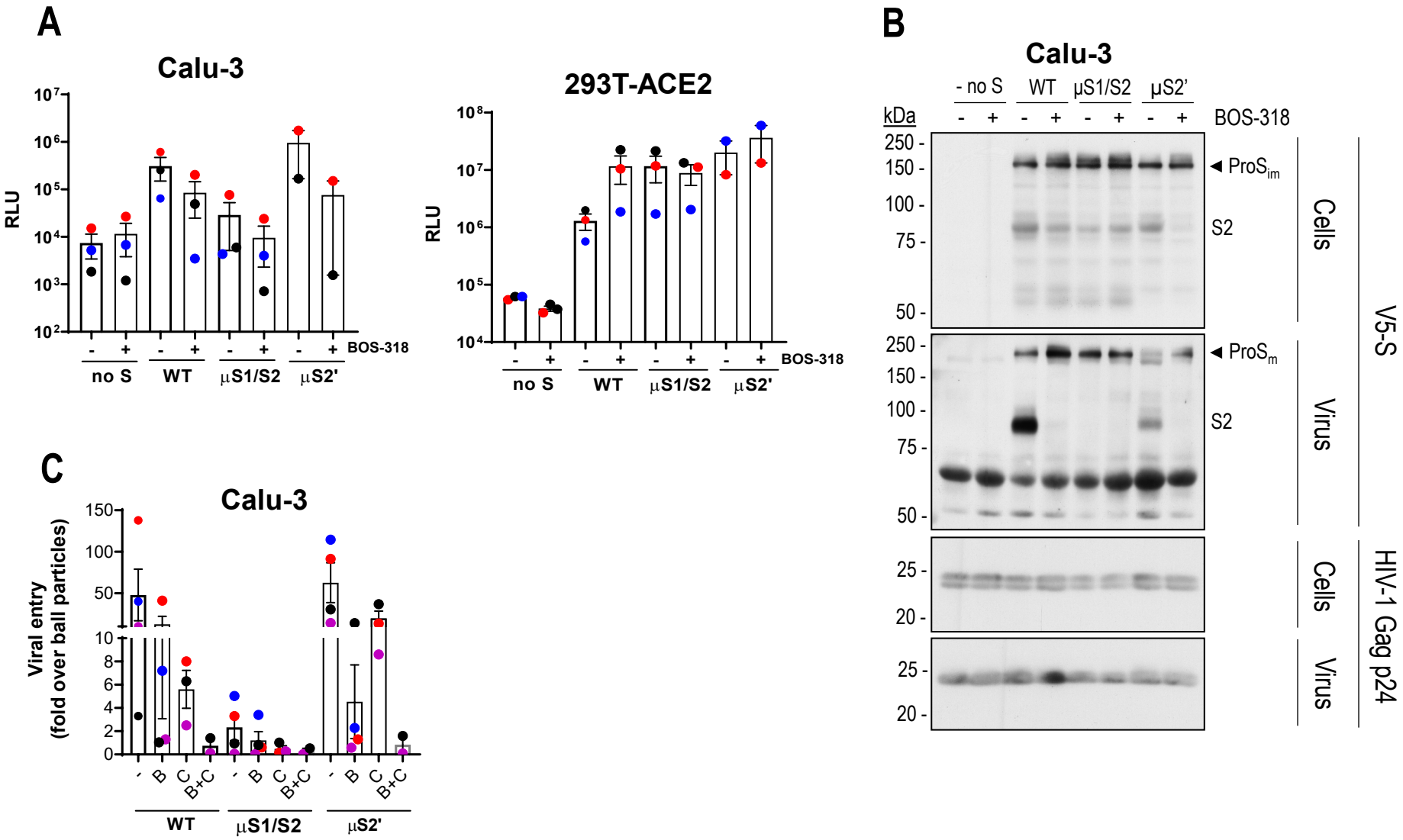
A
Calu-3
RLU
BOS-318
no S
WT
μS1/S2
μS2'
293T-ACE2
B
Calu-3
- no S
WT
μS1/S2
μS2'
kDa
BOS-318
ProS$_{im}$
ProS$_m$
S2
Cells
Virus
V5-S
HIV-1 Gag p24
C
Calu-3
Viral entry
(fold over ball particles)
B
C
B+C

Figure 6: **Processing of SARS-CoV-2 S by Furin-like convertases and TMPRSS2 is critical for viral entry in human lung epithelial cells but not in model HEK293 cells stably expressing ACE2**. (**A**) Furin cleavage of proS at the S1/S2 site is required for SARS-CoV-2 pseudoviral entry in Calu-3 cells but not HEK293T-ACE2 cells. Cells were inoculated with nanoluciferase-expressing HIV particles pseudotyped with SARS-CoV-2: wild-type spike (WT), double Ala-mutant spike (μS1/S2) or Furin-optimized spike (μS2'). Inhibition of proS processing at S1/S2 by a novel Furin-like inhibitor (BOS-318) during pseudovirion packaging prevents viral entry in Calu-3 cells but not in HEK293T-ACE2 cells. (**B**) Western blot analyses show inhibition by BOS-318 of proS processing at S1/S2 site. Purified pseudovirions and cellular extracts of producing HEK293-T17 cells treated or not with BOS-318 inhibitor were separated on SDS-PAGE gel and analyzed for HIV-1 p24 and V5-tagged S-protein (proSm or cleaved, S2) as indicated. (**C**) Pre-treatment of Calu-3 cells with 1 μM BOS-318 (B), 100 μM Camostat (C) or both (B+C) markedly reduces viral entry. In Panels A and C, Calu-3 cells were transduced with nanoluciferase-expressing HIV particles pseudotyped with SARS-CoV-2 S WT, μS1/S2 or μS2' for 72h and analyzed for nano-luciferase expression. Viral entry was expressed as fold increase over that given by bald particles (pseudovirions made in the absence of S). Each dot represents a different experiment with median luciferase activity calculated from three biological replicates. Two to four experiments were performed for each cell type. Error bars indicate standard deviation (SD) from the mean.

Figure 7

A

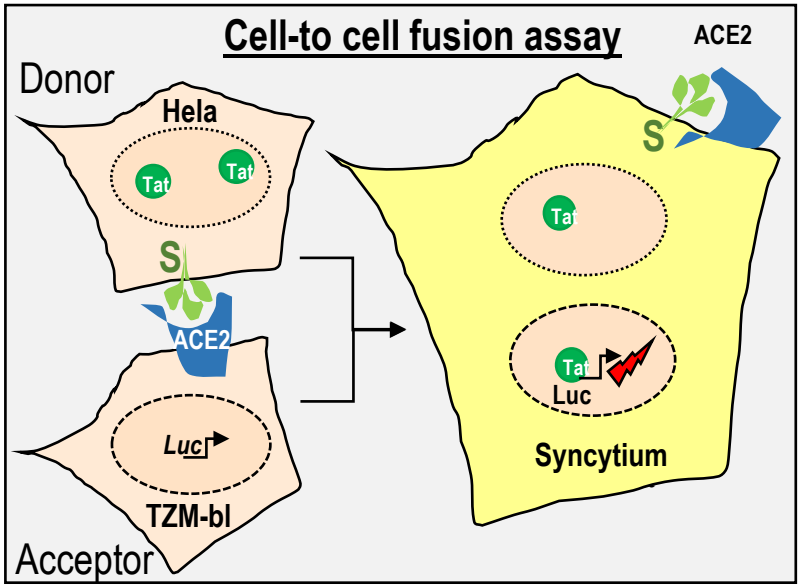

B

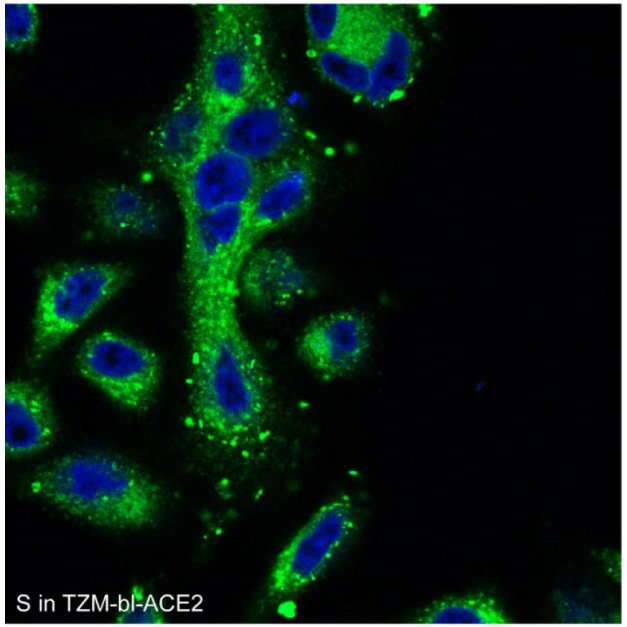

C

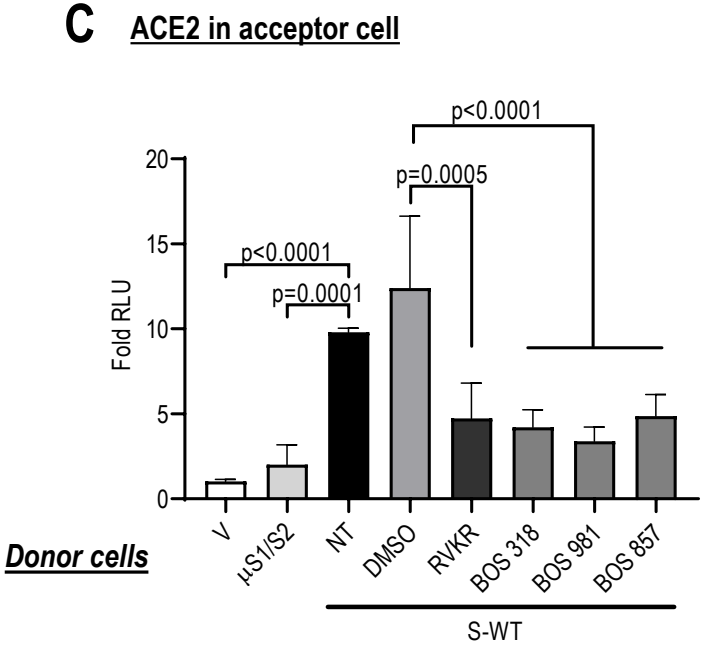

D

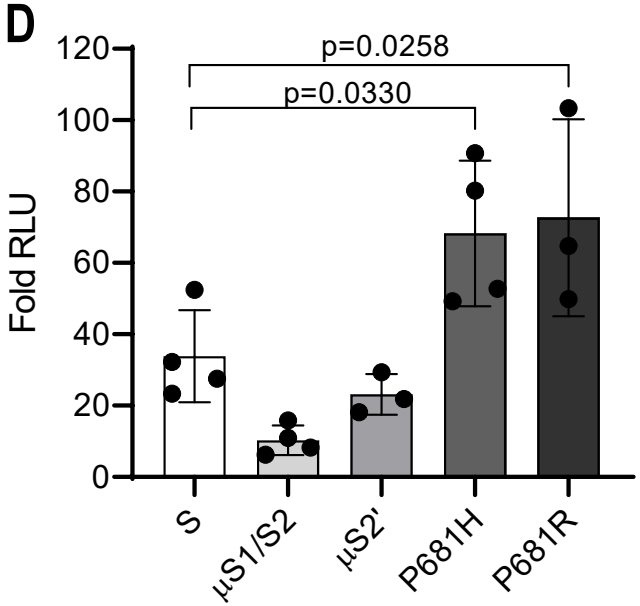

Figure 7: **Spike-induced cell-to-cell fusion relies on Furin cleavage at S1/S2.** (**A**) Cell-to-cell fusion between donor cells (HeLa) expressing the fusogenic SARS-CoV-2 spike protein along with the HIV trans-activator Tat, and acceptor cells (TZM-bl) that express ACE2. Upon fusion, Tat is transferred from donor to acceptor cells, thereby inducing luciferase expression. (**B**) Cell-to-cell fusion was evaluated using confocal microscopy. A representative immunocytochemistry of Hela cells transfected with a vector expressing SARS-CoV-2 spike co-cultured with TZM-bl cells for 18h. The number of syncytia (multiple nuclei) was examined using CellMask™ to probe for the plasma membrane and Dapi to stain the nuclei. (**C**) Donor cells were transfected with vectors expressing either no protein (empty vector, V), μS1/S2, or WT-spike (S) in the absence (NT) or presence of vehicle (DMSO) or with the Furin-inhibitors BOS-318, BOS-981, BOS-857 (300 nM) or RVKR (10 μM). Acceptor cells were transfected with a vector expressing ACE2. After 48h, donor and acceptor cells were co-cultured for 18h. Relative luminescence units (RLU) were normalized to the V value arbitrarily set to 1. Data are presented as mean values ± SD (n=3), One-Way ANOVA, Dunn-Sidàk multiple comparison test. (**D**) Donor HeLa cells expressing WT-S or its indicated mutants and variants were co-cultured with acceptor TZM-bl cells expressing ACE2. The extent of fusion is represented as a ratio between the RLU measured for each condition and that of donor cells expressing empty vector. The bar graph represents the average of 4 experiments performed in triplicates. Data are presented as mean values ± SEM (n=3 or 4), One-way Anova Dunnett's multiple comparison test.

Figure 8

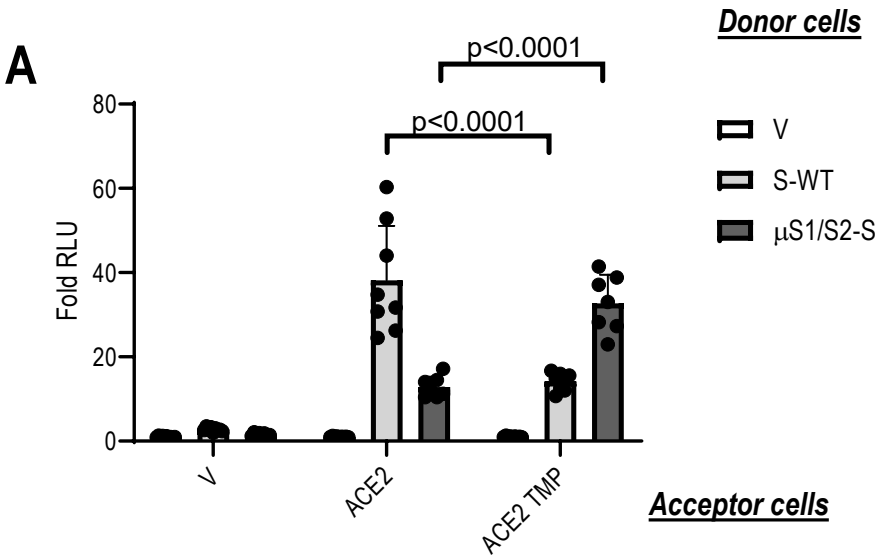
A
Donor cells
p<0.0001
p<0.0001
80
60
40
20
0
Fold RLU
V
S-WT
μS1/S2-S
V
ACE2
ACE2 TMP
Acceptor cells

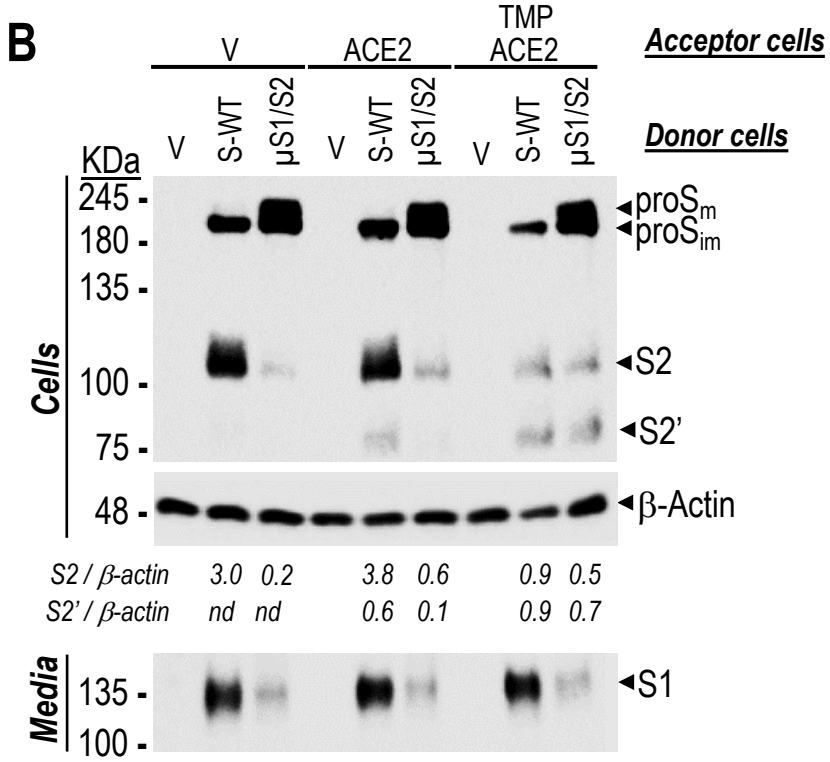
B
Acceptor cells
V
ACE2
TMP ACE2
Donor cells
V
S-WT
μS1/S2
V
S-WT
μS1/S2
V
S-WT
μS1/S2
KDa
245
180
135
100
75
48
Cells
proSm
proSim
S2
S2'
β-Actin
S2 / β-actin 3.0 0.2 3.8 0.6 0.9 0.5
S2' / β-actin nd nd 0.6 0.1 0.9 0.7
Media
135
100
S1

Figure 8: **Spike-glycoprotein processing by Furin and TMPRSS2 in a co-culture system and their role in cell-to-cell fusion.** Donor HeLa cells expressing empty vector (V), WT-S-HA or μS1/S2-HA were co-cultured with acceptor TZM-bl cells expressing V, ACE2 + V, or ACE2 + TMPRSS2. From the same experiment, cell-to-cell fusion (**A**) was assessed in parallel with spike processing in cells and media by Western blotting (**B**). (**B**) spike-glycoproteins in the cell extracts were analyzed by Western blotting using an anti-V5 mAb. Secreted forms of spike protein (S1) in the media were detected with anti HA-HRP upon immunoprecipitation with anti-HA agarose. The bar graph represents the average of 3 experiments performed in triplicates. Data are presented as mean values ± SD Two-way Anova Turkey's multiple comparison test. The corresponding Western-blot is representative of three independent experiments. Values of S2 and S2' relative to β-actin are shown (nd = too low or not detected).

Figure 9

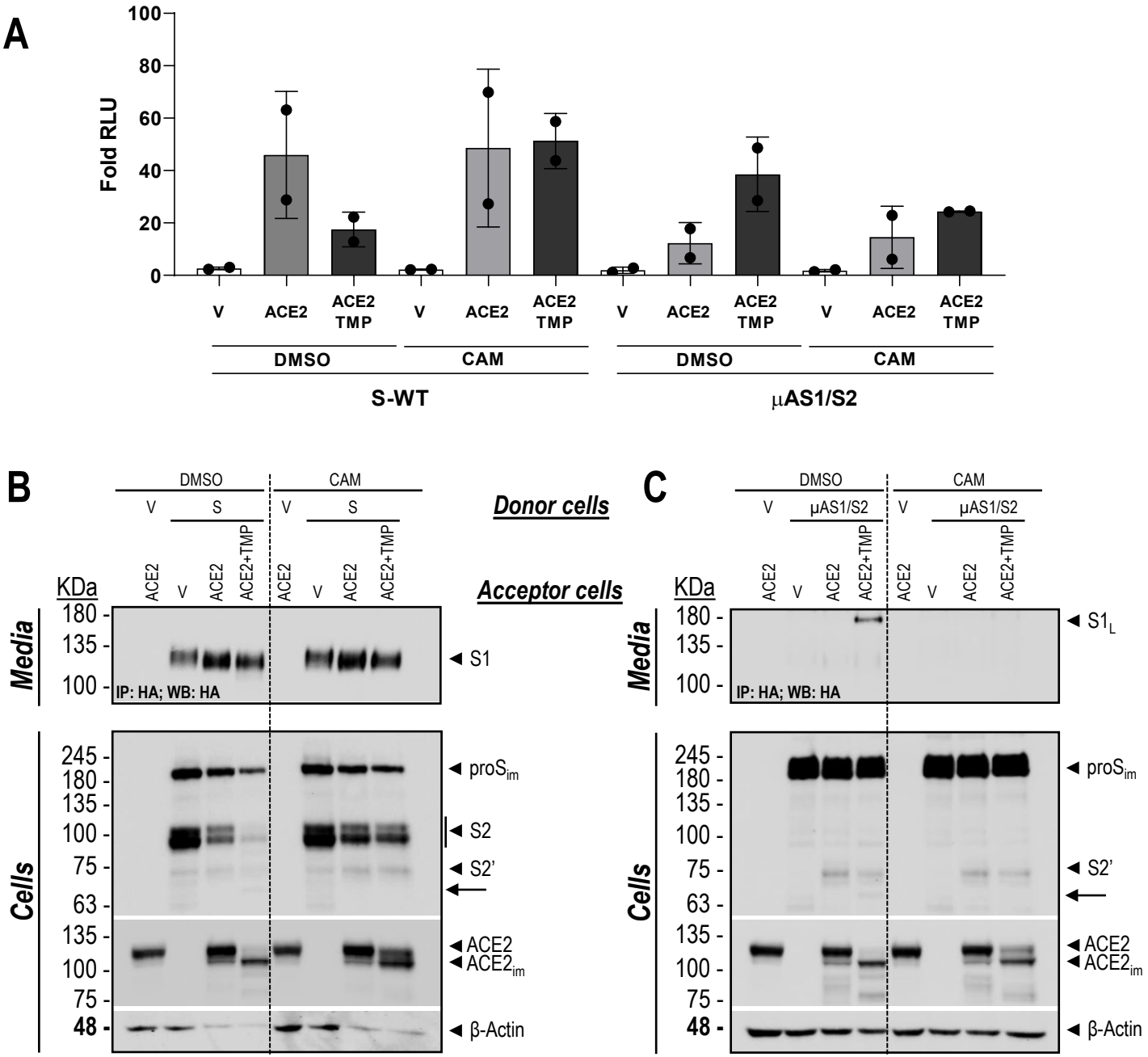
A
Fold RLU
100
80
60
40
20
0
V
ACE2
ACE2 TMP
DMSO
CAM
S-WT
μAS1/S2
B
C
Donor cells
Acceptor cells
KDa
Media
Cells
IP: HA; WB: HA
S1
S1L
proSim
S2
S2'
ACE2
ACE2im
β-Actin
ACE2+TMP
μAS1/S2

Figure 9: **Exogenous TMPRSS2-generated shedding of ACE2 differentially regulates S-induced fusion at the plasma membrane of WT-S *versus* µAS1/S2.** Donor HeLa cells expressing double tagged (N-terminal HA-tag; C-terminal V5-tag) spike-glycoprotein WT (S) or its S1/S2 mutant (µAS1/S2) were co-cultured with acceptor TZM-bl cells expressing (empty vector, V), ACE2 + V, or ACE2 + TMPRSS2 and treated with DMSO (vehicle control) or Camostat (120µM). Within the same experiment, cell-to-cell fusion (**A**) was assessed in parallel with spike processing in cells and media by Western-blot (**B, C**). (**A**) The extent of fusion is represented as a ratio between the RLU measured for each condition and that of donor cells expressing V. The bar graph represents the average of 2 experiments performed in triplicates. (**B, C**). Western blot analyses of media and cell extracts of the co-cultured cells with donor cells overexpressing double tagged (N-terminal HA-tag; C-terminal V5-tag) spike-glycoprotein, WT (S) (**B**) or µAS1/S2 (**C**). The arrow points to a putative degradation product of S2', that is absent in presence of Camostat. Media were subjected to immunoprecipitation with anti-HA agarose for the secreted forms of spike protein (S1, $S1_L$) followed by Western blotting with anti HA-HRP. spike-glycoproteins in the cell extracts were immunoblotted with anti-V5 mAb. The data are representative of three independent experiments.

Figure 10

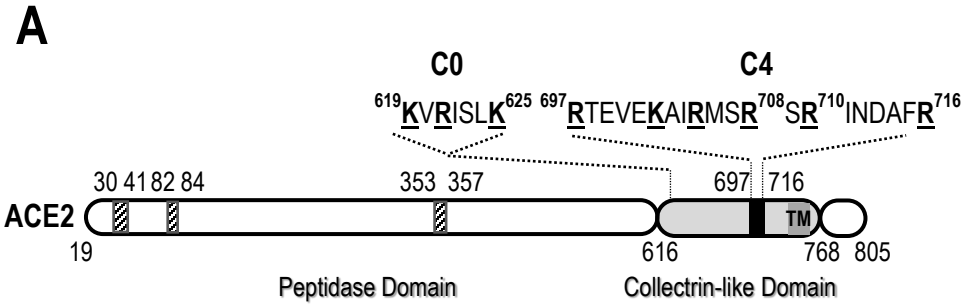
A
C0
C4
619KVRISLK625 697RTEVEKAIRMSR708SR710INDAFR716
30 41 82 84
353 357
697 716
ACE2
TM
19
616
768 805
Peptidase Domain
Collectrin-like Domain

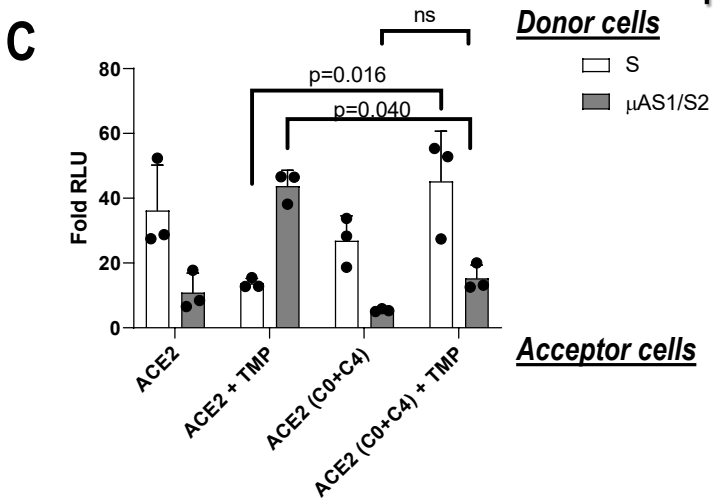
C
Donor cells
S
μAS1/S2
ns
p=0.016
p=0.040
Fold RLU
80
60
40
20
0
ACE2
ACE2 + TMP
ACE2 (C0+C4)
ACE2 (C0+C4) + TMP
Acceptor cells

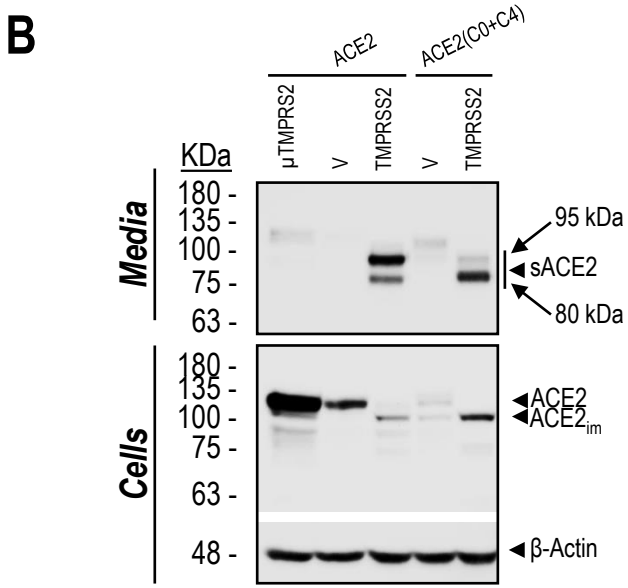
B
ACE2
ACE2(C0+C4)
μTMPRS2
V
TMPRSS2
V
TMPRSS2
KDa
Media
Cells
180
135
100
75
63
48
95 kDa
sACE2
80 kDa
ACE2
ACE2im
β-Actin

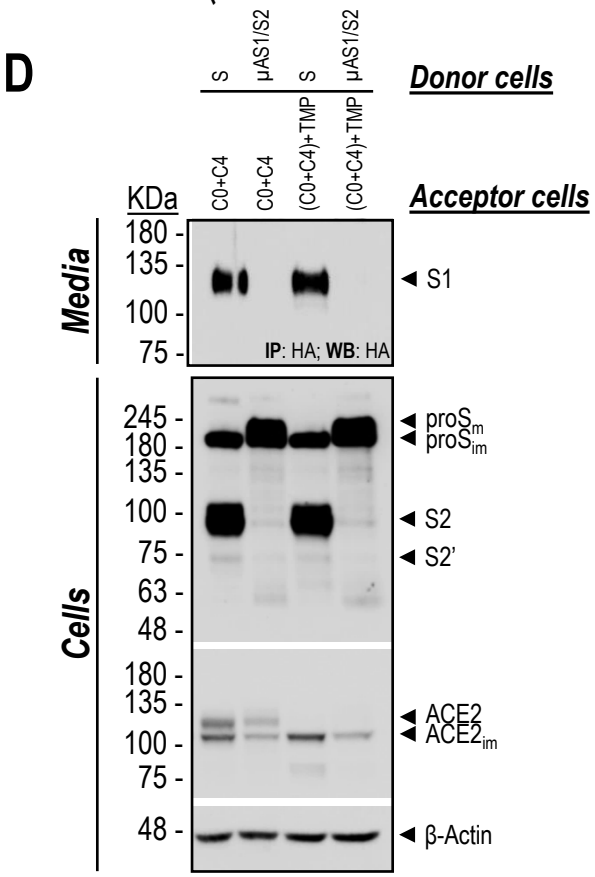
D
S
μAS1/S2
S
μAS1/S2
Donor cells
C0+C4
C0+C4
(C0+C4)+TMP
(C0+C4)+TMP
Acceptor cells
KDa
Media
Cells
180
135
100
75
63
48
245
S1
IP: HA; WB: HA
proSm
proSim
S2
S2'
ACE2
ACE2im
β-Actin

Figure 10: **The C-terminal collectrin-like domain of ACE2 may be critical for the regulation of cell-to-cell fusion of spike-glycoprotein when exogenous TMPRSS2 is present.** (**A**) Schematic representation of the primary structure of human ACE2 with emphasis on the C-terminal collectrin-like domain (aa 616-768, light grey), TMPRSS2 cleavage region (aa 697-716, black) and the polybasic amino-acid segments in which K/R were mutated to A (C0 and C4) (amino acids underlined and in bold). Also shown are the peptidase domain (aa 19-615, white) containing the regions involved in the interaction with the spike SARS-CoV protein (hatched) and transmembrane domain (TM). (**B**) HeLa cells were co-transfected with ACE2, WT (ACE2) or its mutant ACE2 (C0+C4), and TMPRSS2, WT (TMPRSS2) or its S441A active-site mutant (μTMPRSS2), or empty vector (V). Media and cell extracts were analyzed by western blotting for shed ACE2 (sACE2) and ACE2, respectively. The migration positions of the ~95 kDa and ~80 kDa sACE2 are emphasized. (**C**) Donor HeLa cells expressing WT-S-HA or μAS1/S2-HA were co-cultured with acceptor TZM-bl cells expressing ACE2, WT (ACE2) or its mutant ACE2 (C0+C4) in presence or absence of TMPRSS2. From the same experiment, cell-to-cell fusion was assessed (**C**), in parallel with WB analyses of cells and media (**D**). The extent of fusion is represented as a ratio between the RLU measured for each condition and that of donor cells expressing an empty vector. The bar graph represents the average of 3 experiments performed in triplicates. Data are presented as mean values ± SD (n=3), One-way Anova Turkey's multiple comparison test. (**D**) Co-culture media were subjected to immunoprecipitation with anti-HA agarose for the secreted forms of spike protein (S1) followed by western blot with anti HA-HRP. spike-glycoproteins in the cell extracts were immunoblotted with anti-V5 mAb. The Western blot data are representative of three independent experiments.

Figure 11

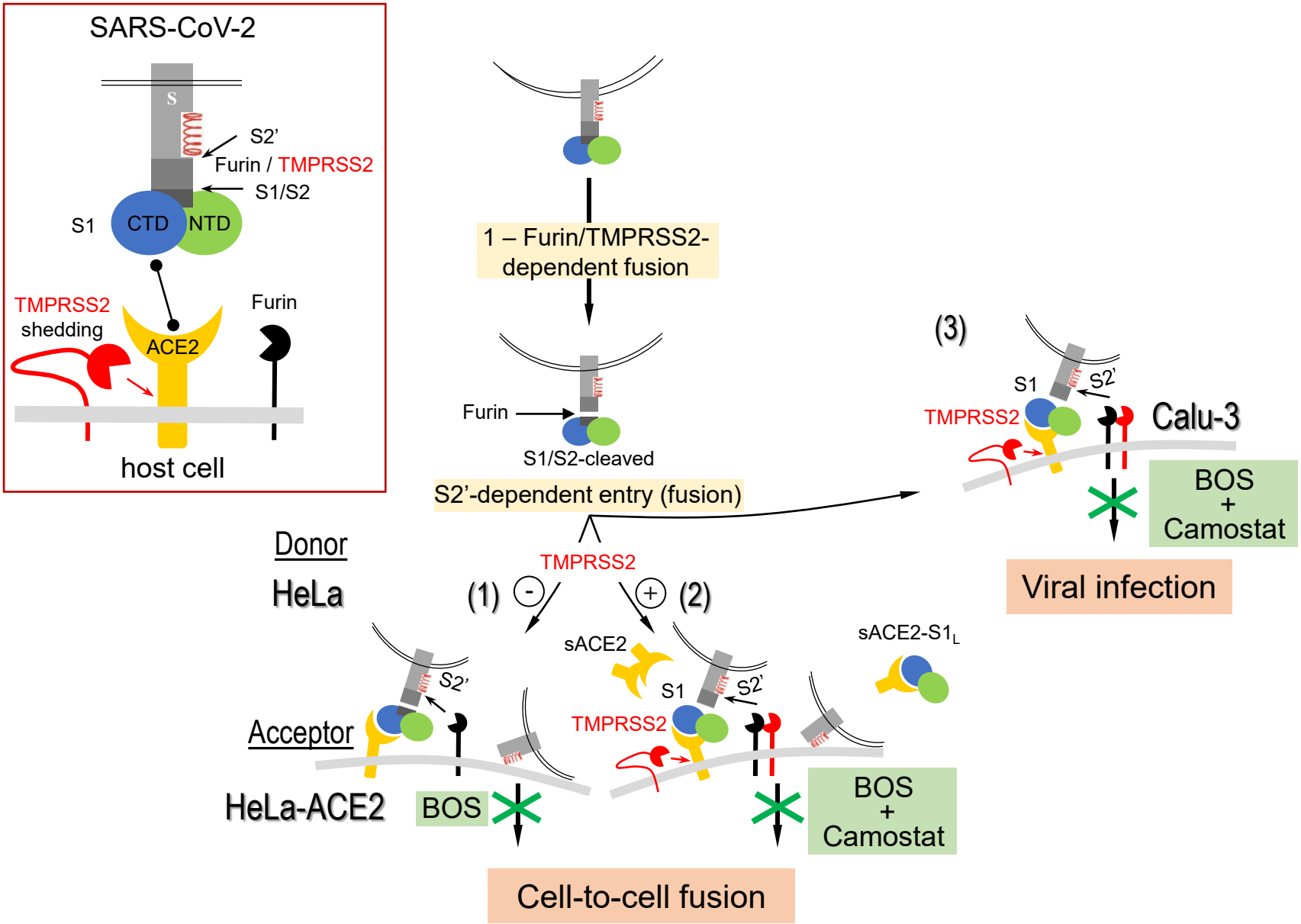
SARS-CoV-2
S
S2'
Furin / TMPRSS2
S1/S2
S1
CTD
NTD
TMPRSS2
shedding
ACE2
Furin
host cell
1 – Furin/TMPRSS2-dependent fusion
Furin
S1/S2-cleaved
S2'-dependent entry (fusion)
(3)
S1
S2'
TMPRSS2
Calu-3
BOS
+
Camostat
Viral infection
Donor
HeLa
TMPRSS2
(1)
(2)
sACE2
sACE2-S1L
S2'
S1
S2'
TMPRSS2
Acceptor
HeLa-ACE2
BOS
BOS
+
Camostat
Cell-to-cell fusion

Figure 11: **Proposed model for the processing of S-protein and its blockade by Furin and TMPRSS2 inhibitors.** Boxed left panel: Schematic representation of the S-glycoprotein domains of SARS-CoV-2, including the N-terminal (NTD) and C-terminal (CTD) domains of S1, the Furin-S1/S2 and the Furin/TMPRSS2-S2' processing sites as well as the fusogenic α-helix that follows S2'. Binding of the RBD domain of S1 to the membrane associated ACE2 in target cells, and the cell surface expression of TMPRSS2 and Furin are also schematized. Right panels: **(1)** BOS-inhibitors (or μS1/S2 mutant) completely prevent cell-to-cell fusion of donor Hela cells expressing S-glycoprotein with acceptor HeLa-ACE2 cells, which lack endogenous TMPRSS2. In this context, this reveals that Furin is a major processing enzyme cleaving at S1/S2 and generating S2'. **(2)** In acceptor HeLa cells expressing TMPRSS2 (+), maximal prevention of cell-to-cell fusion can be achieved by a combination of Furin (BOS, phenocopying the μS1/S2 or μAS1/S2 mutants) and TMPRSS2 (Camostat) inhibitors blocks S2' production, ACE2-shedding (sACE2) and the separation of sACE2-S1L complex from S2. **(3)** Optimal blockade of SARS-CoV-2 infection of Calu-3 cells, which express endogenously both Furin and TMPRSS2, is also achieved by a combination of Furin (BOS) and TMPRSS2 (Camostat) inhibitors.